UNIVERSITY OF OSLO
Department of Chemistry

Nitrogen defects in oxides

Thesis for the Master of Science degree in Materials, Energy and Nanotechnology

Jonathan M. Polfus

June 2009

Preface

This thesis concludes the work for the Master of Science degree under the program for *Materials, Energy and Nanotechnology* at the Department of Chemistry, University of Oslo. The line of study, *Nanotechnology*, reflects the courses that were chosen as a part of the degree and is not specifically related to the topic of the thesis. The experimental work was conducted at the Center for Materials Science and Nanotechnology (SMN) in the time period from August 2007 to June 2009.

I would like to thank my supervisors, Professor Truls Norby and Associate Professor Reidar Haugsrud, for enthusiasm and guidance toward important aspects of both theoretical and practical nature.

I am very grateful to the entire research group and especially Harald Fjeld and Tor Bjørheim for rewarding discussions throughout the past two years. Camilla Vigen is thanked for a pleasant atmosphere in the office and much needed socializing during the last weeks. I would also like to thank Martin Sunding, Claus Nielsen and Hans Normann for help with characterization methods.

Finally, I would like to thank my family and friends for much appreciated support along the way.

University of Oslo, June 2009

Jonathan M. Polfus

Abstract

Defect chemical investigations aimed at describing the influence of nitrogen in oxides are sparse, especially experimental work conducted under equilibrium conditions. In this respect, continued research is necessary to provide insight into novel doping processes and to address the consequences of utilizing ammonia as an energy carrier in fuel cells based on solid oxide electrolytes.

In the present work, the role of nitrogen defects in oxides is investigated by *in-situ* electrical characterization of oxide samples equilibrated in ammonia atmosphere. In this respect, RE_2O_3 (RE = Nd, Gd, Er, Y), RE_6WO_{12} (RE = Gd, Sm), ZrO_2, TiO_2 and ZnO were studied in a 600–1200 °C temperature range. Conductivity measurements of the RE_2O_3 compounds and Y-doped ZrO_2 showed similar conductivities when equilibrated in ammonia as in a H_2/Ar mixture of the same p_{O_2}. However, upon replacing ammonia with an inert gas, the conductivity increases abruptly, typically one order of magnitude. A defect model based on dissolution and dissociation of effectively neutral N-H complexes, $NH_O^\times$, is proposed to describe this behaviour. According to this model, conductivity measurements are interpreted in terms of nitrogen acceptors which are passivated by hydrogen under reducing conditions, and subsequently compensated by positive charge carriers in inert atmosphere as out-diffusion of hydrogen produces an effective acceptor, N_O'. Further conductivity measurements suggest that $NH_O^\times$ and N_O' exist in an equilibrium which can be readily shifted by altering p_{H_2}.

GPA-MS analysis of a Y_2O_3 sample quenched in ammonia from 1200 °C confirm the presence of both nitrogen and hydrogen in the structure, in accordance with the proposed defect model. The concentration of

N was quantified to 0.13 at % by assuming N-H complexes as the only nitrogen and hydrogen related defects. Furthermore, nitride defects were detected in the oxide structure of ZnO and Y-doped ZrO_2 by XPS and quantified to 2.9–5.2 at % and 3.5 at %, respectively. The nitrogen quantification of Y_2O_3 and Y-doped ZrO_2 was found to be in semi-quantitative agreement with the conductivity data when interpreted with the proposed defect model.

In the case of rutile TiO_2, a TiO—TiN solid solution, $TiO_{0.64}N_{0.36}$, was identified by XRD. Moreover, XRD data from ammonia treated ZrO_2 and Gd_6WO_{12} indicate formation of oxynitride phases previously described in literature, $Zr_7O_8N_4$ and $Gd_{3.43}W_{0.57}O_{4.3}N_{1.7}\square_2$, respectively.

Table of Contents

List of Figures

List of Tables

Chapter 1

Introduction

1.1 Oxides and nitrides

Oxides comprise a vast group of compounds that include crystalline phases of practically all metallic and semiconducting elements. Combined with a substantial solid solubility range for many oxides, the result is almost endless combinations of multinary metal–oxide systems. This diversity in both constituents and crystallographic arrangement, makes oxides host for a wide range of properties.

Although not as abundant, nitrides also represent a large group of materials. Due to the lower electronegativity of nitrogen with respect to oxygen, nitride compounds are materials of a more covalent character and generally contain cations in a lower oxidation state than oxides. In terms of properties, they are often characterized as refractories which implies high mechanical strength and chemical stability. The standard free energy of formation of oxides (per mole cation) is generally more negative than those of nitrides [1]. Combined with the reactive nature of oxygen, this makes nitrides prone to oxidation, but many are kinetically stable even at intermediate temperatures.

1.2 Nitrogen in oxides

Considering the electronegativity of nitrogen and the size of the nitride ion, it is reasonable to assume that nitrogen in an oxide will behave in much of the same way as oxygen. By this argumentation, nitride ions on oxygen and interstitial sites will predominate the defect structure. N^{3-} is isoelectronic with O^{2-} and the ionic radius of the nitride ion is only $\sim$5.8 % larger than that of the oxygen ion (table 1.1). Taking into account the higher polarizability of the nitride electron cloud, the lattice strain induced by substitutional nitride ions should not be of significance for dilute concentrations of nitrogen. However, phase transition into an oxynitride[1] is often a results of the formation of oxygen vacancies in addition to the nitrogen substituents.

Table 1.1: *Some properties of the oxygen and nitrogen atom/ion. Radii apply for four-fold and six-fold coordination for negative and positive ions, respectively [2]. Electronegativity is given in Pauling scale.*

	Oxygen	**Nitrogen**
Anionic radius	1.38 Å	1.46 Å
Cationic radius (+3/+5)	—	0.16 / 0.13 Å
Electronegativity	3.44	3.04
Electron configuration	$1s^2 2s^2 2p^4$	$1s^2 2s^2 2p^3$

In contrast to oxygen, nitrogen can also exist in positive oxidation states, where +3 and +5 are most stable. The small size of these cations makes interstitial positions most probable. In this respect, association with oxygen by forming NO complexes may be energetically preferred in some materials.

Many oxides dissolve significant amounts of hydrogen in the form of protons. The protons often reside within the electron cloud of oxygen, and the protonic defect can then be more accurately described as hydroxide

[1] An oxynitride contains structurally arranged oxygen, nitrogen and/or oxygen vacancies in the anionic network.

ions. Similarly, association between protons and nitride ions is another nitrogen related defect that may be of importance.

1.3 Doping — cations and anions

Doping (*i.e.* dissolution of aliovalent foreign atoms) is an eminent method of enhancing electrical and optical properties of semiconductors and insulators. In this process, the electroneutrality condition is exploited to promote the formation of charged defects. Thus, dopants can be compensated by, for instance, electrons, holes, oxygen vacancies or protons, which make them extensively used in functionalized ceramics.

Due to ease of fabrication, stability and predictability, the doping strategy of oxides is predominated by the use of cations. However, in some cases, cation dopants are found to not behave as expected or give undesirable side effects. In zinc oxide, difficulty in achieving reliable *p*-type conduction is usually related to the formation of intrinsic donors such as zinc interstitials or oxygen vacancies, rather than holes. In this respect, acceptor doping on the anion sublattice with chalcogenides, especially nitrogen, show promising results [3]. Moreover, in the search for novel materials for heterogeneous photocatalysis, anion doping of TiO_2 shows beneficial properties over cations due to lower probability of charge carrier recombination [4,5] and enhanced thermal stability [6]. Other situations in which anion doping can be preferred over cations include low solubility of the dopant or if the dopant level is situated close to the middle of the band gap and is not easily activated.

1.4 Motivation and method

Detailed understanding of nitrogen defects and its influence on the properties of oxides is still in its infancy. Although there is an increased interest in doping oxides with nitrogen, there are, to the author's knowledge, no reports on electrical characterization under equilibration with a nitrogen source. Thus, the aim of this work is to investigate

whether such measurements may give insight into the defect structure and properties of nitrogen in oxides.

The primary method of characterization is high temperature *in-situ* electrical conductivity measurements of oxide samples equilibrated in nitriding atmospheres. In this respect, effects of ammonia and N_2/H_2 mixtures are investigated in comparison with purely reducing conditions. Furthermore, as this study revolves around the defect chemical behaviour of nitrogen in oxides, it is desirable to retain the oxide structure. In other words, formation of nitrides or oxynitrides are not of particular interest. Results from conductivity measurements are supported by *ex-situ* characterization methods such as XRD, SEM, XPS and GPA-MS. The compounds that have been investigated are

- binary rare-earth sesquioxides: RE_2O_3 (RE = Nd, Gd, Er, Y)
- binary transition metal oxides: TiO_2, ZnO, ZrO_2
- ternary rare-earth tungstates: RE_6WO_{12} (RE = Sm, Gd)

These compounds are chosen with respect to effects of nitrogen defects rather than specific applications. However, this study is conducted in a context of material research for energy conversion devices (*e.g.* fuel cells, gas separation membranes, opto-electronic devices *etc.*). Of particular interest are the consequences of using ammonia as an energy carrier in solid oxide fuel cells, especially with respect to whether nitrogen defects can influence the overall performance or versatility of such fuel cells.

Chapter 2

Theory

Theory for defect chemistry and conductivity is based on *Defects and Transport in Crystalline Solids* by Kofstad and Norby [7] while theory presented in the section about doping is based on *Solid State Electronic Devices* by Streetman and Banerjee [8], whenever specific references are not given.

2.1 Defects in crystalline solids

The third law of thermodynamics states that the entropy of a system at 0 K is well defined and constant. Furthermore, the system must exist in the ground state at absolute zero. The entropy of the system is then determined only by the degeneracy of the ground state.

A perfect crystal[1] represents a unique ground state configuration of atoms and can only exist at 0 K. This implies, in accordance with the third law of thermodynamics, that such a crystal has zero entropy. At all other temperatures, defects are spontaneously formed in the crystal structure. This process mainly reflects the large gain in entropy associated with creating defects in a perfect structure.

Figure 2.1 shows the local and configurational contributions to Gibbs energy of a crystal as function of the number of point defects it contains. It is the nonproportionality of the configurational entropy, S_{conf}, with

[1] A hypothetical single crystal that is infinitely large *i.e.* without surface atoms.

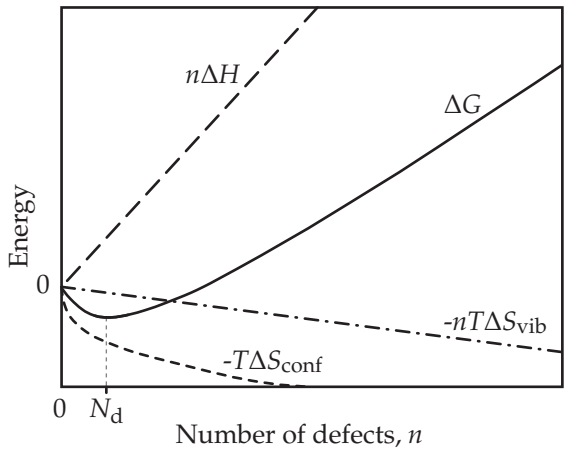

Figure 2.1: *Contributions to Gibbs energy of a crystal as a function of the number of point defects,n, with the perfect crystal as reference. The enthalpy of formation, ΔH, and the vibrational entropy, ΔS_{vib}, refer locally to the individual defect. ΔS_{conf} is the configurational contribution and is not proportional to the number of defects. N_{d} represents the equilibrium concentration of defects.*

respect to the number of defects that permits a finite equilibrium concentration of defects, N_{d} [9]. This concentration is given by the minimum in ΔG where $\frac{\mathrm{d}\Delta G}{\mathrm{d}N_{\mathrm{d}}} = 0$ as shown in the figure. However, although defects may be thermodynamically favorable, kinetics might hinder their formation resulting in the crystal being in a non-equilibrium state. Furthermore, it must be emphasized that the enthalpy of a defect reaction can be negative if the reaction involves consumption of a less stable defect.

The fact that defect formation reactions are entropy driven results in a temperature dependency in which defect solubility increases with temperature. Nevertheless, in comparison to the total number of sites in the crystal, equilibrium concentrations of defects are usually low but some compounds can accommodate considerable amounts of non-stoichiometry.

Defects in crystalline materials are often classified by whether they occupy a point, a line, a plane, a volume or if they are delocalized in the structure. Point defects, or 0-dimensional defects, are those which are

associated with a single site in the crystal. Typical point defects are foreign atoms and dopants, vacancies, valence defects and interstitial species. Electrons in the conduction band and holes in the valence band are typical delocalized defects. In this work, it is the point defects and delocalized defects that are relevant.

2.1.1 Kröger-Vink notation

The *defect structure* of a compound is a complete description of the type and concentration of all point and electronic defects as a function of the activities of the constituents and temperature.

In order to describe defects in an efficient manner, Kröger and Vink [10] devised a notation that relates the position and charge of a defect to the perfect structure. The general formula for a defect is then written A_S^z, where A is an element or a vacancy, S is the site it resides on and z is the effective charge. Effective charge is the charge of species A relative to the charge of the species on site S in the perfect structure. Effective charges are denoted with a superscipt bullet, $^\bullet$, slash, $^/$, or cross, $^\times$, for positive, negative and neutral charges, respectively.

The integer number of charge of all species does not imply that the compounds are treated as purely ionic. The effective charge simply represents the number of electrons that are associated with the defect. The charge can then be distributed around the site of the defect in a covalent manner.

2.1.2 Defect reactions and equilibria

Defect chemical reactions consider the formation and/or annihilation of defects. The criteria for writing defect reactions are

Mass balance The mass of the reactants and products must be equal. Electronic defects are usually, for reasons of simplicity, not considered in the mass balance.

Electroneutrality Electroneutrality requires that the charge of the reactants equals the charge of the products. Equivalently, the effective

charge can be considered instead. The electroneutrality condition can be expressed mathematically as the sum over the concentrations of all charged species, S, multiplied by their charge, z

$$\sum_{S} z[S^z] = 0 \tag{2.1}$$

Conservation of site ratio The site ratio of the host structure must be conserved. Interstitial positions are omitted from the site ratio.

Although a material will contain many different defects, only a few will predominate in a particular compound at a given temperature and chemical condition. In the case of oxides, the defect situation depends on the partial pressure of oxygen in the surrounding atmosphere. Typical defects are oxygen interstitials or metal vacancies, and oxygen vacancies or metal interstitials, which dominate at high and low p_{O_2}, respectively.

In the following, reactions for the formation of nitrogen defects are proposed for oxides in general. Dissolution of nitrogen onto an oxygen site from nitrogen gas can be written

$$N_2(g) + 3O_O^{\times} = 2N_O^{\prime} + v_O^{\bullet\bullet} + \tfrac{3}{2}O_2(g) \tag{2.2}$$

and the corresponding equilibrium constant, K, is given by

$$K = [N_O^{\prime}]^2 \, [v_O^{\bullet\bullet}] \, p_{N_2}^{-1} \, p_{O_2}^{3/2} \tag{2.3}$$

It should be noted that this nitridation reaction has a stronger dependency on the partial pressure of oxygen than that of nitrogen.

Reaction 2.2 is in competition with dissolution of negative interstitial nitrogen

$$N_2(g) + 3O_O^{\times} = 2N_i^{\prime\prime\prime} + 3v_O^{\bullet\bullet} + \tfrac{3}{2}O_2(g) \tag{2.4}$$

where oxygen vacancies are chosen as the charge compensating defect. Whether the substitutional or interstitial defect will predominate depends on their relative formation energy. Furthermore, it is reasonable to assume that interstitial nitride ions are favorable under nitriding conditions in materials which favor oxygen interstitials under oxidizing conditions.

Thus, nitrogen and oxygen interstitials also compete and both may in principle predominate under different activities of nitrogen and oxygen. The relevance of positive interstitials will be addressed in chapter 3.2.

Similar reactions can be written with ammonia as the nitrogen source and water as a product

$$2NH_3(g) + 3O_O^{\times} = 2N_O^{/} + v_O^{\bullet\bullet} + 3H_2O(g) \tag{2.5}$$

$$2NH_3(g) + 3O_O^{\times} = 2N_i^{///} + 3v_O^{\bullet\bullet} + 3H_2O(g) \tag{2.6}$$

The equilibria of these reactions are, however, more complicated due to the preferential formation of N_2 and H_2 rather than ammonia when the reaction proceeds to the left.

2.1.3 Doping

The purpose of a dopant is to either donate or accept one or more electrons from the structure. Whether a dopant is a donor or acceptor depends on its effective charge, and thus is related to the crystallographic site it occupies. In elemental compounds, dopants can be interstitial or substitutional but the situation becomes more complex as the number of aliovalent elements in the compound increases.

In general, dissolution of dopants shifts the defect situation from an intrinsic to an extrinsic region when the concentration surpasses a certain threshold level. This is illustrated as a function of the concentration of acceptor dopant in figure 2.2. Considering the full electroneutrality, which can be

$$[N_O^{/}] + n = 2[v_O^{\bullet\bullet}] + p \tag{2.7}$$

acceptors will suppress the concentration of negative defects and promote the concentration of positive defects.

Dopants introduce discrete electron energy levels within the band structure. Shallow acceptor and donor levels are defined as within $\sim 3kT$ of the valence band maximum and conduction band minimum, respectively. Deep levels are situated close to the middle of the band gap and thus have a higher ionization energy. It should be noted that

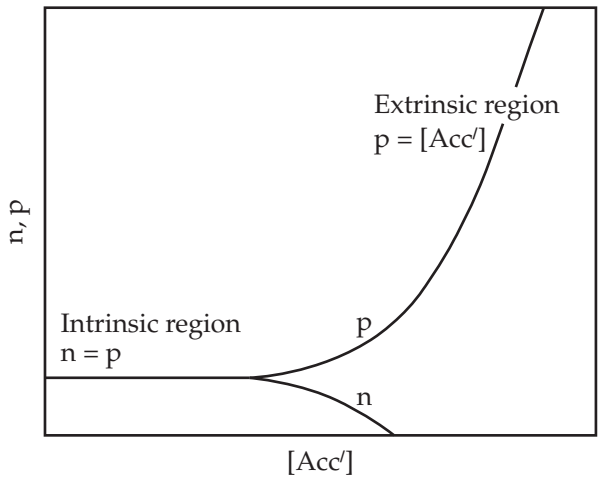

Figure 2.2: *Transition from an intrinsic to an extrinsic defect situation upon increasing dopant concentration for a compound where acceptors are compensated by electron holes. Edited from Kofstad and Norby [7].*

substitutionally dissolved aliovalent foreign atoms are not necessarily dopants. This can be the situation for a foreign element with an excess electron at an energy level close to the valence band.

Electrical activation of the dopant typically occurs by thermal excitation of an electron from a donor into the conduction band (figure 2.3(a)), or from the valence band to an acceptor (figure 2.3(b)). However, if an acceptor and a donor co-exist, the excess electron of the donor will be depleted by the acceptor without introducing any electronic charge carriers to the bands. This concept can also include intrinsic defects *i.e.* a foreign atom acceptor compensated by an oxygen vacancy[2] (figure 2.3(c)). Similarly, cation vacancies and anion interstitials are typical intrinsic acceptors, while cation interstitials usually act as donors.

As for all fermions, the electron occupancy of the energy states in the band diagram is determined by Fermi-Dirac statistics. The probability that an orbital at energy E will be populated is given by the Fermi-Dirac

[2]The energy level of an oxygen vacancy donor, $v_O^{\times}$, is not always situated within the band gap, it may also reside within the conduction band [11].

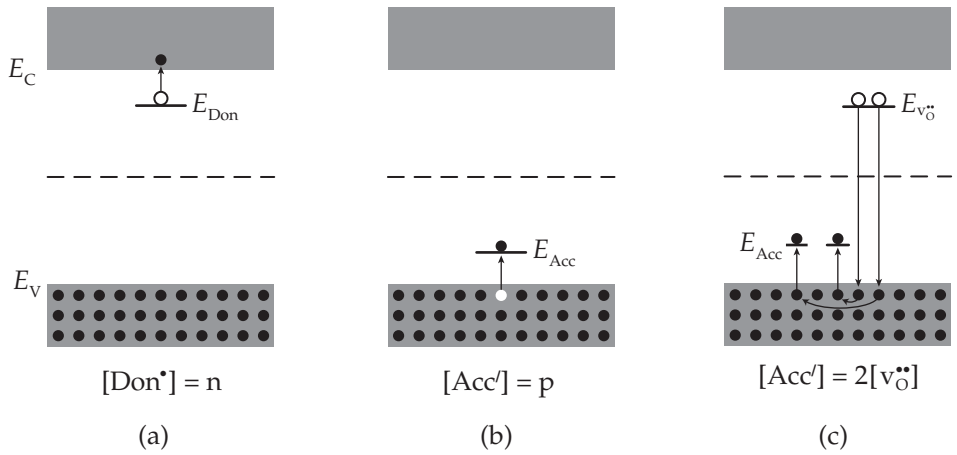

Figure 2.3: *Band diagrams with dopant levels for a) n-type doping, b) p-type doping and c) dopant compensated by an intrinsic defect.* E_V *and* E_C *denotes the band edge of the valence band and conduction band, respectively. The concentration of charge carriers is governed by electroneutrality as written below the diagrams.*

distribution formula

$$f(E) = \frac{1}{\exp\left(\frac{E-E_F}{kT}\right) + 1} \tag{2.8}$$

where E_F is the Fermi level and k is Boltzmann's constant. The Fermi level describes the concentration of electrons in the conduction band and holes in the valence band and from equation 2.8, it can be seen that $f(E_F) = 0.5$. Thus, in an intrinsic semiconductor, the Fermi level is a pseudo level close to the middle of the band gap, with a shift proportional to the difference in the density of states in the conduction band and valence band. Furthermore, depending on the concentration and placement of dopant levels, the Fermi level will increase in a donor doped system, and decrease in an acceptor doped system. As a consequence, dopants can be amphoteric, that is, be a donor or acceptor depending on the Fermi level of the system *e.g.* hydrogen in various semiconductors [12].

2.2 Electrical conductivity

The electrical conductivity of a resistive material is proportional to the charge, concentration and mobility of all charge carriers in the material. The partial conductivity for species i, σ_i, is then written

$$\sigma_\mathrm{i} = z_\mathrm{i} \mathrm{e} c_\mathrm{i} u_\mathrm{i} \tag{2.9}$$

where $z_\mathrm{i}\mathrm{e}$ is the charge, c_i is the concentration and u_i is the charge carrier mobility. The total conductivity, σ_Tot, can be described as the sum of the partial conductivities for the different species

$$\sigma_\mathrm{Tot} = \sum_\mathrm{i} \sigma_\mathrm{i} \tag{2.10}$$

Diffusion of ionic charge carriers in polar materials (*e.g.* oxides) proceed according to an activated hopping mechanism. The self diffusion coefficient of species i, D_i, can then be related to conductivity and charge carrier mobility through the Nernst-Einstein relation

$$\frac{D_\mathrm{i}}{\mathrm{k}T} = \frac{u_\mathrm{i}}{z_\mathrm{i}\mathrm{e}} = \frac{\sigma_\mathrm{i}}{c_\mathrm{i}(z_\mathrm{i}\mathrm{e})^2} \tag{2.11}$$

Accordingly, mobility, and in turn conductivity, follows an Arrhenius type behaviour

$$\sigma_\mathrm{i} = \frac{\sigma_0}{T} \exp\left(-\frac{\Delta H_\mathrm{a}}{\mathrm{k}T}\right) \tag{2.12}$$

where σ_0 is the pre-exponential factor and ΔH_a is the activation energy for conduction. The latter is determinded by the enthalpy of formation, ΔH_f, and mobility, ΔH_m, of the charge carrier

$$\Delta H_\mathrm{a} = \Delta H_\mathrm{f} + \Delta H_\mathrm{m} \tag{2.13}$$

The pre-exponential involves terms related to the charge, concentration and vibration frequency of the diffusing species, symmetry of the structure, jump distance and entropy of formation and transport. However, if the charge carrier concentration is constant and independent of temperature (*e.g.* determined by a dopant), the enthalpy and entropy of formation are excluded from the activation energy and pre-exponential, respectively.

The driving force for net charge transport can be electrical and/or chemical potential gradients, $z_\mathrm{i}\mathrm{e}\frac{d\phi}{dx}$ and $\frac{d\mu_\mathrm{i}}{dx}$, respectively, in 1-dimension. The resulting current density of species i, i_i, then becomes

$$i_\mathrm{i} = -\frac{\sigma_\mathrm{i}}{z_\mathrm{i}\mathrm{e}}\left(\frac{d\mu_\mathrm{i}}{dx} + z_\mathrm{i}\mathrm{e}\frac{d\phi}{dx}\right) \tag{2.14}$$

2.2.1 Polarons

Free electrons or holes will polarize the local atomic environment and distort the structure of ionic and covalent crystals. This distortion will accompany the electron/hole, and thus reduce its mobility. The inseparable combination of the electron and the strain field it induces can be viewed as a quasi-particle, and is then called a polaron.

Depending on the amount of electron–lattice interactions, polarons can be large or small. For large polarons, lattice polarization is small and the electron moves in a band, but with an enhanced effective mass. Mobility then follows a temperature dependence of $T^{-1/2}$ at high temperatures and activation energies are typically small (~ 0.1 eV) [13].

If the electron interacts strongly with the lattice, and the polaron is smaller than the lattice parameter, it is said to be a small polaron. In this case, the polaron is more localized and most of the time trapped at a single lattice site. At low temperatures, the electron tunnels slowly through the crystal, as if in a band of large effective mass. At high temperatures the electron moves from site to site by an activated hopping process which gives an Arrhenius type conductivity as described in equation 2.12. In comparison to band conduction, mobility is greatly reduced and activation energies can be 0.5 eV or higher [13].

The small polaron model is typical for highly ionic compounds where coloumbic interactions between electrons and ions are strong. On the other hand, the large polaron model typically applies to more covalent materials.

2.3 Van der Pauw 4-point method

Van der Pauw [14,15] derived a method for measuring electrical resistivity and Hall coefficients of disc samples with arbitrary shape.

The van der Pauw method uses four ohmic point electrodes placed at, or as close as possible, to the circumference of a sample. The sample itself has to be of uniform thickness and without isolated holes. These criteria are the basis for calculating the resistivity of the sample without knowing the current pattern through the sample.

Figure 2.4(a) shows a disc sample with four contacts (1, 2, 3 and 4). If a current is passed through the sample from contact 1 to 2, and the potential difference is measured between contact 3 and 4, the corresponding resistance can be calculated using Ohm's law

$$R_{12,34} = \frac{U_{34}}{I_{12}} \tag{2.15}$$

Furthermore, if the contacts are rotated in a clockwise direction, as shown in figure 2.4(b), a second resistance can be measured

$$R_{23,41} = \frac{U_{41}}{I_{23}} \tag{2.16}$$

Van der Pauw showed that the resistances $R_{12,34}$ and $R_{23,41}$ are related to the samples resistivity through

$$\exp\left(-\frac{\pi d}{\rho}R_{12,34}\right) + \exp\left(-\frac{\pi d}{\rho}R_{23,41}\right) = 1 \tag{2.17}$$

where d is the sample thickness and ρ is its resistivity[3]. Equation 2.17 is called the van der Pauw formula. It cannot be solved with the use of normal functions, so the resistivity is often obtained by solving the equation numerically with an iterative method. From equation 2.17 it is clear that any unevenness in the thickness of the sample will result in a deviation from the correct value of the resistivity.

The van der Pauw method is for highly conducting samples often preferred over a 2-point setup since the measured resistance is not

[3]However, if the sample contains a line of symmetry, the contacts can be placed so that $R_{12,34} = R_{23,41}$ and only one measurement is necessary.

influenced by the electrodes. It also allows for high accuracy, especially when combined with reciprocal[4] and reversed polarity[5] measurements. These methods also provide good control of the repeatability of the measurements. Van der Pauw measurements can be used with both AC and DC, and gives the total resistance of the specimen *i.e.* sum of the bulk and grain-boundary resistances.

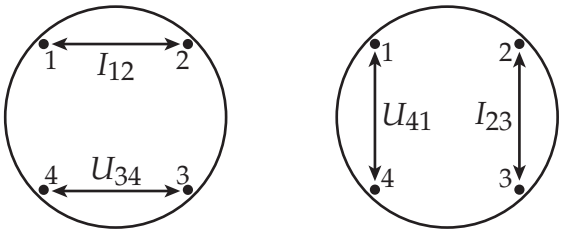

Figure 2.4: *A disc sample with four electrodes for use with the van der Pauw method. The resistance is measured according to Ohm's law for two configurations: a) equation 2.15 and b) equation 2.16.*

2.4 Gas-phase equilibrium of ammonia

Ammonia is in the gas phase at ambient conditions and exists in an equilibrium given by

$$\mathrm{NH_3(g)} \rightleftharpoons \tfrac{1}{2}\mathrm{N_2(g)} + \tfrac{3}{2}\mathrm{H_2(g)} \tag{2.18}$$

Due to the endothermic nature of this reaction, the equilibrium is shifted towards the products by increasing the temperature. Figure 2.5 shows the partial pressures of the constituents in reaction 2.18 at thermodynamic equilibrium as a function of temperature. However, reaction kinetics will prevent the system from reaching equilibrium, at least in the lower temperature range. Furthermore, if a system is continuously

[4]The current and voltage electrodes are interchanged to give the resistance as the average of two measurements.

[5]The polarity of the current source and voltmeter is reversed to average over two measurements.

supplied with ammonia, the effective decomposition rate is reduced and a relatively high partial pressure of ammonia can be obtained even at high temperatures.

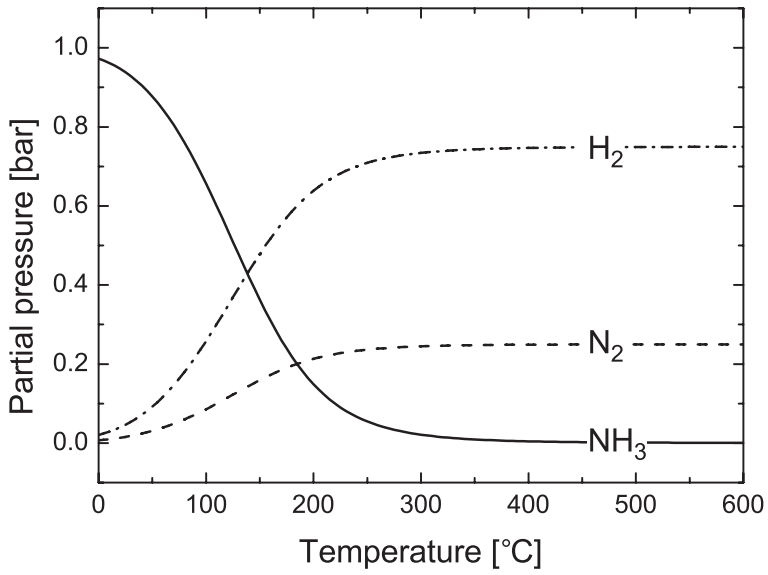

Figure 2.5: *Partial pressure of NH_3, N_2 and H_2 at equilibrium and 1 bar total pressure. Calculated using HSC Chemistry 4.1 [16].*

Chapter 3

Literature

Oxynitrides and nitrogen defects in oxides are investigated for an increasing group of compounds. Detailed insight into the formation and properties of such materials has been pursued through many different approaches and with a widespread of questions and applications in mind. In the following literature review, special attention will be directed towards the material systems, preparation method, type of defects and characterisation methods that have been a part of the present work. As an exception, literature on nitrogen *defects* in TiO_2 will be included as it contributes to the overall understanding of nitrogen in oxides.

The first part is devoted to an overview of the structure, defects and transport properties of the pure and cation doped oxides.

3.1 Defects and transport in relevant oxides

3.1.1 Rare-earth sesquioxides — RE_2O_3

The rare-earth sesquioxides crystallize into different modifications of the fluorite structure termed A, B and C. The relative stability of these modifications vary systematically with the cation radius along the lanthanide series from C $\rightarrow$ B $\rightarrow$ A. At ambient pressure, Nd_2O_3 has the hexagonal A-type structure, Gd_2O_3 has the monoclinic B-type structure, and Er_2O_3 and Y_2O_3 has the cubic C-type structure [17].

Yttrium sesquioxide — Y_2O_3

Tallan and Vest [18] investigated the defect structure of nominally undoped Y_2O_3 by conductivity measurements as a function of p_{O_2} at 1200–1600 °C. Conductivity, shown as a function of p_{O_2} in figure 3.1, is reported to be purely electronic above 1200 °C. Oxygen vacancies compensated by electrons, and yttrium vacancies compensated by holes are proposed to predominate at low and high p_{O_2}, respectively. However, later studies gives evidence of oxygen interstitial being the dominating defect at high p_{O_2} [19–21].

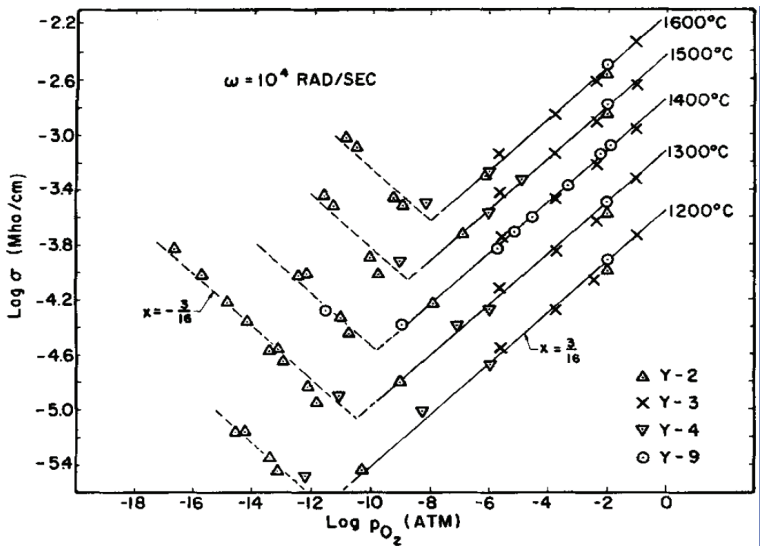

Figure 3.1: *AC conductivity of Y_2O_3 as a function of p_{O_2} as reported by Tallan and Vest [18].*

Katayama *et al.* [22] have investigated the electrical properties of Y_2O_3 as a function of CaO-doping up to 10 mol %. Figure 3.2 shows the conductivity as a function of temperature for various doping concentrations. Based on EMF measurements and p_{H_2O} dependencies, the increase in conductivity with dopant concentration is attributed to formation of holes.

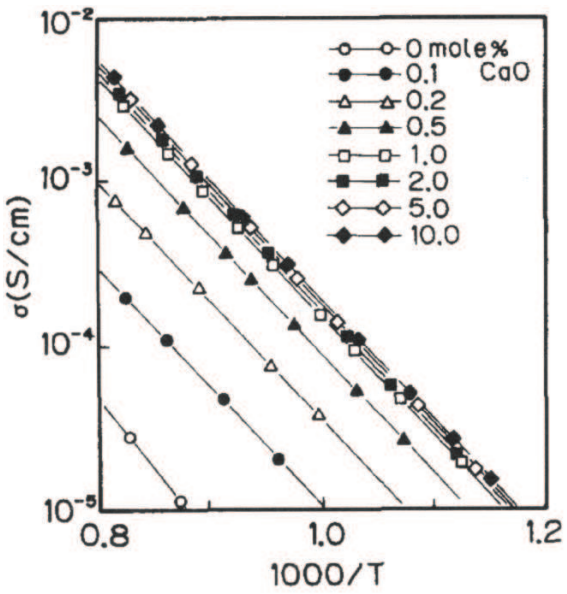

Figure 3.2: *Conductivity of Y_2O_3 as a function of temperature for various CaO concentrations measured in dry air from Katayama et al. [22].*

Er_2O_3, Gd_2O_3 and Nd_2O_3

Reports on detailed electrical characterization of undoped Er_2O_3, Gd_2O_3 and Nd_2O_3 as a function of temperature and p_{O_2} are limited. Based on the review by Kofstad [23] and the collected report by Lal and Gaur [24], it can be asserted that the essential electrical properties of the sesquioxides are quite similar. That is, they exhibit *p*-type and *n*-type conductivity under oxidizing and reducing conditions, respectively, and electronic conduction predominates at high temperatures.

3.1.2 Rare-earth tungstates — RE_6WO_{12}

McCarthy *et al.* [25] have investigated the RE_2O_3—WO_3 system and suggest that the structure of RE_6WO_{12} is related to that of fluorite. The formula is then written $RE_{3.43}W_{0.57}O_{6.85}\square_{1.15}$ according to a fluorite-type formulation, where $\square$ denotes structural anion vacancies. Furthermore, the symmetry of the structure varies with the radius of the rare-earth cation and is reported to be pseudo-tetragonal for RE = Sm, Gd.

The electrical properties of the RE = La, Nd, Gd, Er compounds have been investigated as a function of p_{O_2} and p_{H_2O} by Haugsrud [26]. The effect of acceptor doping with CaO was found to vary with the rare-earth element: conductivity decreased upon doping RE = La, Nd, and increased for RE = Gd, Er. This difference was most prominent at lower temperatures, and negligible above approximately 700 °C for RE = Gd.

The conductivity was found to be *n*- and *p*-type under reducing and oxidizing conditions, respectively, and predominated by oxide ions in between these regimes for RE = Er, Gd.

3.1.3 Zirconium dioxide — ZrO_2

ZrO_2 has a monoclinic structure at room temperature which transforms to tetragonal at 1170 °C and to cubic at 2370 °C [27].

It is well known that the high temperature phases can be stabilized by addition of acceptor dopants through formation of oxygen vacancies. The 3 and 8 mol % yttria stabilized zirconia (YSZ) samples used in the present work are fully stabilized *i.e.* cubic at RT. Because of the large concentration of vacancies and relatively low concentration of electronic defects, these oxides exhibit nearly complete ionic conductivity over a large range of oxygen partial pressures and temperature [28].

Vest *et al.* [29] found that monoclinic ZrO_2 shows a minimum in conductivity at about 10^{-16} bar p_{O_2} at 1000 °C, and *n*- and *p*-type conductivity at lower and higher p_{O_2}, respectively.

3.1.4 Titanium dioxide — TiO_2

TiO_2 exists in three modification where the tetragonal rutile phase is the most stable. While the defect structure of rutile TiO_2 is extensively studied, literature is inconsistent as to which defects that account for oxygen deficiency. In this respect, Kofstad [28] has reviewed reports on conductivity and non-stoichiometry in rutile and proposed two regimes where oxygen vacancies and cation interstitials predominate at high and low p_{O_2}, respectively. Furthermore, the transition between these defect

situations shifts to lower p_{O_2} with decreasing temperature, which is in agreement with a later review by Millot *et al.* [30].

Rutile is an *n*-type semiconductor where charge transport proceeds according to the band model [31], *i.e* non-activated mobility (section 2.2).

3.1.5 Zinc oxide — ZnO

ZnO is a direct wide band gap semiconductor ($E_g \sim 3.3\,eV$) which possesses the hexagonal wurtzite structure under ambient conditions. Specimens of nominally undoped ZnO are found to be *n*-type, but the reason for this is still under controversy. The intrinsic donors $v_O^\times$ and $Zn_i^\times$ have been proposed to account for the *n*-type behaviour [32]. However, first principles studies by Kohan *et al.* [33], Janotti and van de Walle [34,35] indicate that these defects, in addition to $Zn_O^\times$, are deep donors and/or have too high formation energies to be expected to exist in significant quantities.

Due to its high solubility, shallow donor level, and presence in many growth techniques, hydrogen is proposed as a possible cause for the *n*-type behaviour of ZnO [36].

3.2 Reactions and kinetics of nitridation

Preparation of partially nitrided oxides can be seen as divided into two groups: synthesis with a nitrogen precursor and treatment of the bare oxide. Furthermore, these reactions can occur at equilibrium, or be more kinetically controlled such as many thin-film processes and ion-implantation. In the present work, oxide samples are treated with ammonia under equilibrium conditions.

Reducing conditions is an important prerequisite for substitutional incorporation of nitrogen. This is because the activity of oxygen must be sufficiently low in order to remove oxygen from the structure and for the nitrogen substituent to be stable *i.e.* avoid reoxidation. Particularly, when nitrogen acceptors are compensated by oxygen vacancies, the

equilibrium constant for nitrogen dissolution has a stronger dependency on the activity of oxygen than that of nitrogen (equation 2.3).

For the nitridation of an oxide through gas phase equilibrium in a reducing atmosphere, Elder *et al.* [1] claim that the formation of water is the main driving force[1] [1]. Expressed in defect chemical terms, such a reaction with nitrogen gas as the nitrogen source can be written

$$N_2(g) + 3H_2(g) + 3O_O^{\times} = 2N_O^{/} + v_O^{\bullet\bullet} + 3H_2O(g) \tag{3.1}$$

and similarly for ammonia

$$2NH_3(g) + 3O_O^{\times} = 2N_O^{/} + v_O^{\bullet\bullet} + 3H_2O(g) \tag{3.2}$$

The enthalpies of these reactions differ only by the relative stability of ammonia compared to nitrogen and hydrogen gas. Furthermore, the entropy gain is more favorable for reaction 3.2 due to the increase in the number of moles of gas. However, as will become clear in the following, the main difference between these reactions in practice lies with kinetics. First of all, the triple bond of the N_2 molecule is among the strongest in nature (942 kJ mol^{-1}). In comparison to the N-H bond energy in ammonia, 386 kJ mol^{-1}, it is clear that a direct reaction between nitrogen gas and an oxide would require much higher temperature and catalytic activity than an equivalent reaction with ammonia, to occur at similar rates.

In this respect, Cheng *et al.* [37] report that the nitridation process was clearly accelerated when zirconia was reacted with ZrN rather than N_2(g) up to 2000 °C. Chung *et al.* [38] have explained similar experiments up to 1700 °C in terms of nitridation kinetics that are controlled by diffusion in the case of ZrN and by interface reaction in the case of N_2(g).

Valov [39] has conducted experiments with electrochemical incorporation of nitrogen into YSZ with both nitrogen and ammonia gas. It was determined that electrode kinetics, and not the diffusion of N into bulk, was rate limiting for nitriding a single crystal with nitrogen gas up to 700 °C. A substantially lower voltage was required with ammonia as the nitrogen source, indicating that the reaction was not kinetically hindered in this

[1] Reduction of Gibbs energy.

case. This was explained by the oxidation state of nitrogen in the nitrogen source: ammonia contains nitrogen in the same formal oxidation state as in the oxide *i.e.* N^{3-}, thus avoiding the redox step which is necessary in the case of nitrogen gas. Based on Valov's results, one may anticipate the absence of nitrogen defects in positive oxidation states with ammonia as the nitrogen source due to the >3-step oxidation that is required.

3.3 Structure and phase relationships

3.3.1 Zirconium oxynitrides

Partial nitridation of zirconia occurs at temperatures above 900 °C at ambient pressures, leading to the formation of zirconium oxynitride phases from the ZrO_2 rich part of the ZrO_2—Zr_3N_4 system. Nitrogen dissolves substitutionally for oxygen, creating a negative defect compensated by oxygen vacancies.

This was first investigated by Gilles *et al.* [40] who studied the reaction of ZrO_2/ZrN mixtures in the presence of nitrogen or ammonia at temperatures of 900–2000 °C. Three oxynitride phases were observed: β, β' and γ, which were identified as $Zr_7O_8N_4$, $Zr_7O_{11}N_2$ and Zr_2ON_2, respectively. Cheng and Thompson [41] observed an additional phase, $\sim Zr_7O_{9.5}N_3$ (β''), when ZrO_2 was reacted with nitrogen gas at 1400–2000 °C under reducing conditions. All the observed oxynitride phases can be described by the general formula $ZrO_{2-2x}N_{4x/3}$ [42], but the exact stoichiometry of the β''-phase is not yet determined [43].

In the case of the β-type structure, the oxide–oxynitride phase transition arises from distortions and ordering of the oxygen vacancies due to strong vacancy–vacancy interactions. Thus, they are closely related to the fluorite-type structure of zirconia, and can be viewed as different superstructures of this [44].

Shaw *et al.* [45] discovered that pre-existing disordered vacancies in YSZ suppressed the formation of oxynitride phases. It was suggested that this was due to the difficulty in ordering the vacancies that were already present due to the yttrium acceptors.

3.3.2 Oxynitrides of rare-earth tungstates

Diot *et al.* [46] have prepared oxynitride phases of various rare-earth tungstates in flowing ammonia. Ammonolysis of RE_6WO_{12} (RE = Nd, Sm, Y, Ho) was carried out in the 700–1000 °C range and the amount of nitrogen incorporation progressively increased with nitridation temperature and time.

In all cases, the substitution of oxygen with nitrogen is accompanied by the formation of oxygen vacancies. The resulting oxynitride solid solution domain ranges from $RE_{3.43}W_{0.57}O_{6.85}\square_{1.15}$ to $RE_{3.43}W_{0.57}O_{4.3}N_{1.7}\square_2$[2]. Interestingly, the maximum nitrogen uptake corresponds to the same amount of vacancies as that of the bixbyite-type stoichiometry ($A_4X_6\square_2$). The bixbyite structure is an anion defect fluorite with structurally ordered vacancies. However, the XRD patterns of these oxynitrides only show, to a first approximation, a cubic $Fm\bar{3}m$ symmetry of a disordered fluorite type structure.

In terms of possible application, the color of the nitrided powders was found to change continuously with the nitrogen content. This continuous variation in the absorption edge position towards higher wavelengths, as characterized by diffuse reflectance spectroscopy, was explained by a decrease in the band gap energy and thus a progressively more covalent character of the material [47].

3.3.3 Solid solubility in TiO—TiN

TiO exists in two polymorphs, whereof one is a heavily defected, non-stoichiometric and disordered NaCl-type structure. TiN can adopt the same cubic structure with a similar lattice parameter ($a_{TiN} = 4.24173$ Å, $a_{TiO} = 4.185$ Å[3]). This structural similarity leads to stable solid solutions of TiO and TiN, or titanium oxynitride. Figure 3.3 shows an isothermal section of a Ti—O—N phase diagram as proposed by Granier *et al.* [48].

[2] $RE_{3.43}W_{0.57}O_{6.85}\square_{1.15}$ and RE_6WO_{12} are equivalent representations of the same compound (section 3.1.2).

[3] From PDF database: TiN 38-1420, TiO 77-2170.

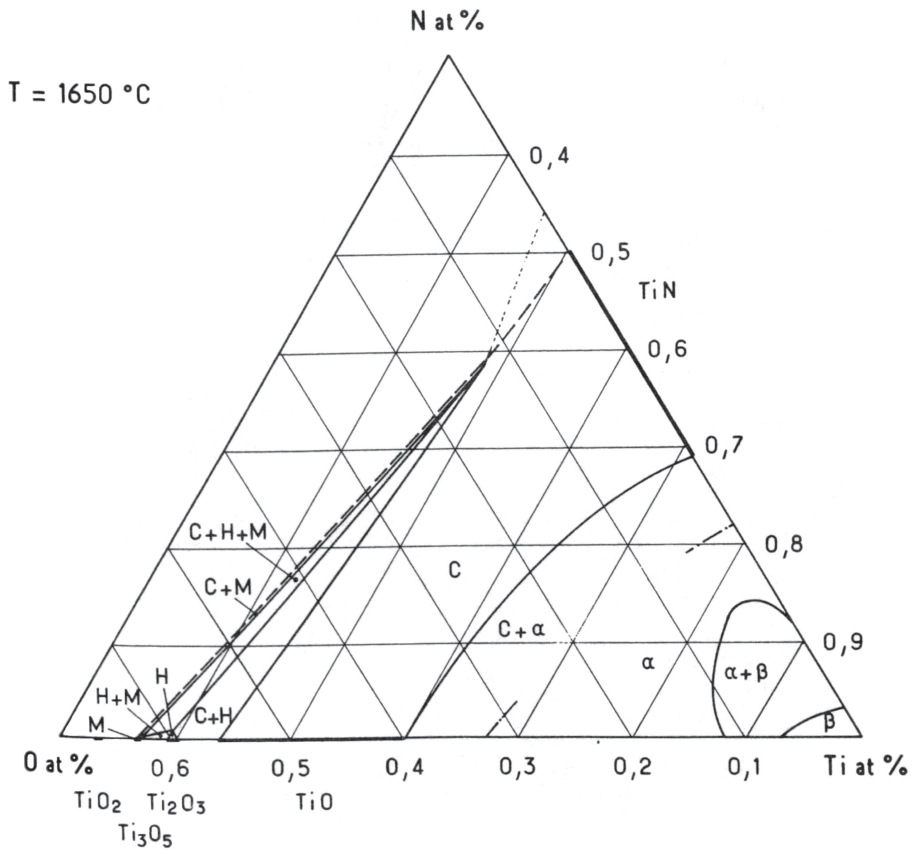

Figure 3.3: *Isothermal section of the ternary phase diagram Ti—O—N as proposed by Granier et al. [48]. The cubic TiO—TiN solid solution, denoted* c*, exists over a quite large stoichiometric range.*

Yang *et al.* [49] have prepared nitrogen rich titanium oxynitride by a thermal liquid-solid metathesis with $TiCl_4$ and NaN_3 precursors at 350 °C. The XRD data of the resulting nanocrystals showed a lattice parameter of 4.236 Å. Vegard's law was applied on the basis of a TiN_xO_{1-x} stoichiometry to give a composition of $TiN_{0.91}O_{0.09}$. By comparison with XPS analysis of both surface and bulk, the TiN_xO_{1-x} stroichiometry was concluded to fit reasonably well.

Regardless of Yangs conclusions, Drygaś *et al.* [50] avoid using Vegard's law on XRD data from similar powders prepared by a two-stage aerosol process with NH_3. The reasoning behind this is in part because of the controversy surrounding the quantitative interpretation of XRD data

for nanopowders, but also due to the non-stoichiometry present in both TiO and TiN and thus most probably in the oxynitride system as well. In this respect, Drygaś argue that the oxynitride composition should be written TiN_xO_y.

3.4 Nitrogen defects

3.4.1 Nitrogen doping of ceria

Jorge *et al.* [51] investigated the incorporation of nitrogen into CeO_2 powder samples, using flowing ammonia gas at temperatures from 400–1100 °C for 17 h. The nitrogen content was determined by combustion analysis and it was found that nitrogen incorporation takes place between 550 and 900 °C. The maximum uptake of 3 at % was observed for a narrow temperature range close to 700 °C. X-ray photoelectron spectroscopy (XPS) analysis of a sample treated at 650 °C confirmed that nitrogen was incorporated into the structure. The XPS spectrum, showed in figure 3.4, contained two contributions in the N 1s region. The peak at 400.1 eV corresponds to molecularly chemisorbed nitrogen on the surface, and the peak at 397.4 eV was assigned to Ce-N bonds. The Ce-N binding energy corresponded quite well with the general binding energy of transition metal nitrides (396–397 eV) and specifically CeN (396.2 eV).

Nitrogen is said to dissolve substitutionally for oxygen, and along with the partial reduction of Ce^{4+} to Ce^{3+}, be compensated by oxygen vacancies.

3.4.2 Nitrogen in TiO_2

Triggered by the work of Asahi *et al.* [52], anion doping is seen as a prominent method of enhancing the photocatalytic properties of TiO_2. The subsequent study of non-metal doping in TiO_2 (B, C, N, F, P, S) is comprehensive. So far, nitrogen seems to be the candidate with the most promising results [4, 5, 53]. However, there is an open debate on the relation between the dopant and the increased photocatalytic properties.

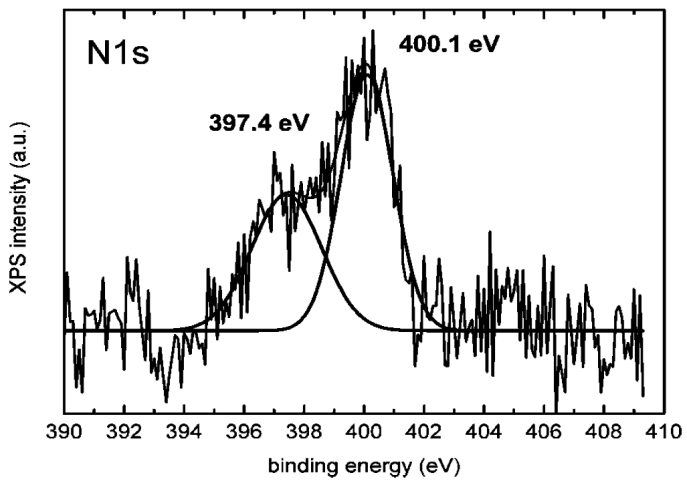

Figure 3.4: *XPS spectrum of the N 1s line of* $CeO_{1.92}N_{0.05}V_{0.025}$*. From Jorge et al. [51].*

Based on considerations of the density of states upon substitution of O by N, Asahi *et al.* [52] have reported a band gap narrowing effect in nitrogen doped anatase. It was concluded that N-2p states were introduced slightly above the valence band maximum, and the valence band shift resulted from mixing of the N-2p states with O-2p states. This should result in a lowering of the optical excitation energy from UV to the visible region, which was confirmed experimentally. However, recent reports suggest that the visible light response in N-doped TiO_2 might be due to isolated N-2p states above the valence band maximum, rather than band gap narrowing [54]. Lindgren *et al.* [55] confirmed not only isolated N-2p states above the valence band, but also that there was no change in the position of the valence band edge. The observed absorption of visible light is then attributed to excitation of electrons from localized N-impurity states to the conduction band.

Kitano *et al.* [56] argue that nitrogen doped TiO_2 can, depending on the concentration of N-substituents, exhibit both isolated N-2p levels and a band gap narrowing. Low nitrogen concentrations (< 2 anion %) resulted in an increased absorption as a shoulder into the visible region, indicating isolated N-2p states. On the other hand, higher nitrogen concentrations

(2–16.5 anion %) resulted in a shift of the whole absorption band into the visible light region (figure 3.5). In this case, steep absorption edges, as opposed to a shoulder, are said to be clear evidence of band gap narrowing.

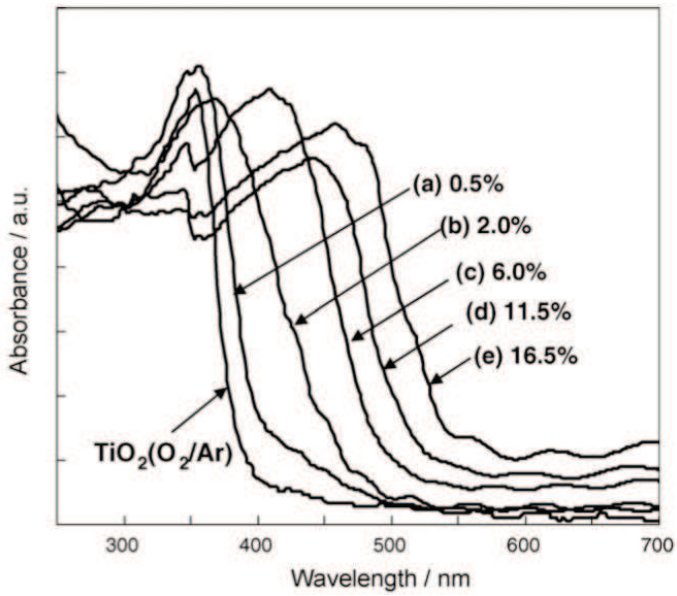

Figure 3.5: *UV-vis absorbance spectrum of pure and doped TiO_2 films from Kitano et al. [56]. The concentration of substitutional nitrogen in the doped specimens (anion %): (a) 0.5, (b) 2.0, (c) 6.0, (d) 11.5, and (e) 16.5.*

Valentin *et al.* [4] investigated nitrogen doped TiO_2 samples prepared via a sol-gel method with electron paramagnetic resonance (EPR)[4] and XPS. Two types of paramagnetic nitrogen species were observed with EPR, whereof one was determined to be a monomeric nitrogen specie incorporated in the bulk structure. However, these results could not be correlated with XPS results, where nitrogen related peaks partially or completely disappeared after careful washing of the sample surface.

Work by the same group also includes density functional theory (DFT) calculations on substitutional and interstitial nitrogen in the anatase

[4]EPR is a highly accurate an sensitive spectroscopy technique for investigating paramagnetic species *i.e.* species with one or more unpaired electrons.

structure. Substitutional nitrogen was found to exist as N^{3-} while in the interstitial configuration of lowest energy, nitrogen was in a positive oxidation and bound to one lattice oxygen. Calculations on the electronic structure indicated virtually no shift in the valence band or conduction band edges. Due to the low nitrogen concentrations of up to ∼1 %, this is still in accordance with the work of Kitano *et al.* [56] mentioned earlier. As illustrated in figure 3.6, substitutional nitrogen introduces localized N-2p states slightly above the valence band. In contrast, the interstitial N-O defect gives rise to occupied π-states below the valence band and partially occupied antibonding π^*-states above the valence band. In both cases, nitrogen is an acceptor. A detailed analysis of the spin properties was performed for comparison with the experimental EPR results. In conclusion, both the interstitial and substitutional nitrogen could account for the paramagnetic species observed experimentally.

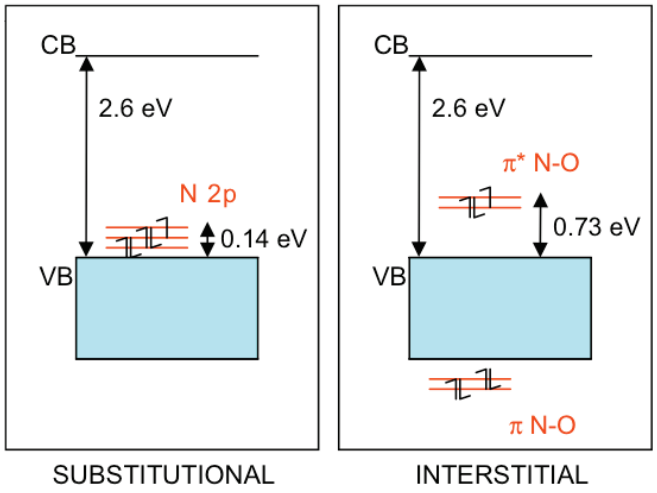

Figure 3.6: *Positions of substitutional and interstitial nitrogen in the band structure of anatase TiO_2 from Valentin et al. [4].*

Relationship with oxygen vacancies

Valentin *et al.* [4] also investigated the relationship between substitutional nitrogen ions and oxygen vacancies in the anatase TiO_2-lattice by means

of DFT modeling. It was discovered that the formation energy for oxygen vacancies was drastically reduced in the presence of nitrogen impurities, from 4.2 eV in pure anatase to 0.6 eV in N-doped anatase. Figure 3.7 illustrates how substitutional nitrogen in combination with oxygen vacancies become increasingly favorable at low oxygen pressures.

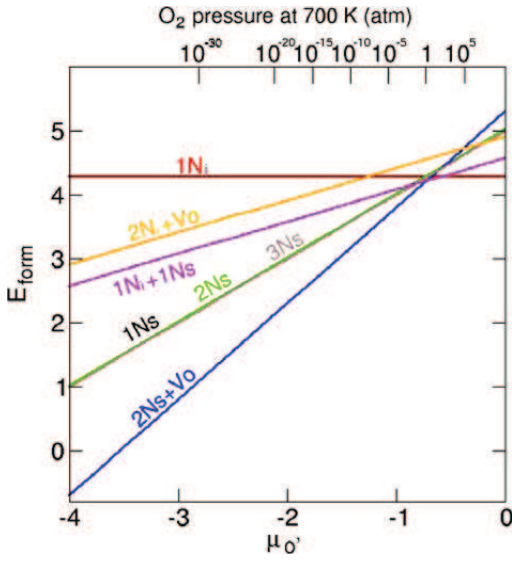

Figure 3.7: *Stability diagram for combinations of substitutional nitrogen, Ns, and interstitial nitrogen, Ni, in the presence of oxygen vacancies, Vo. From Valentin et al. [4].*

These considerations are supported by the work of Batzill *et al.* [57] through a combined XPS/UPS and STM[5] study on the surface properties of nitrogen doped anatase and rutile. In addition, results indicate that the oxygen vacancies are mobile and not bound to the nitrogen acceptors.

3.4.3 N-H complexes

Li *et al.* [58] have investigated the role of hydrogen in nitrogen-doped ZnO using Fourier transformed infrared (FTIR) absorption and *ab-initio* DFT calculations. Nitrogen-doped ZnO thin films were fabricated using low-pressure metal-organic chemical vapor deposition (MOCVD) with

[5]Scanning Tunneling Microscopy.

diethylzinc and dilute NO gas as precursors. Hydrogen and nitrogen concentrations were determined using secondary-ion mass spectrometry[6] and XPS, respectively. Nitrogen levels were found to be in the range of 1–3 at %. Hydrogen levels were found to vary with the diethylzinc flow rate, suggesting that the hydrogen originated from the precursor.

DFT was used to calculate the formation energies of a H_i defect, a N_O defect and a NH_O complex. Figure 3.8(a) shows the calculated formation energies, and illustrates that an associated N-H complex has lower formation energy than the sum of the isolated N_O and H_i defects. As shown in figure 3.8(b), N-H complexes were proposed by FTIR analysis in accordance with the theoretical predictions.

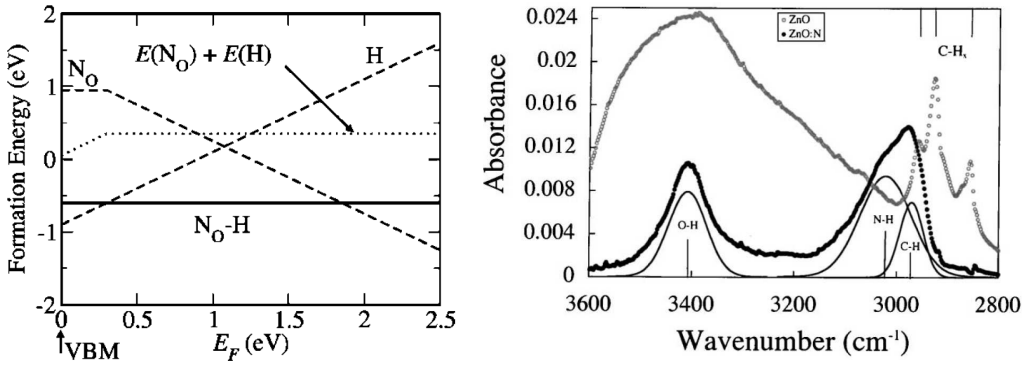

(a) (b)

Figure 3.8: *a) Formation energy for* N_O, H_i *and the sum of these,* $N_O + H_i$, *compared with the formation energy of an* NH_O *complex. b) FTIR spectrum showing N-H stretch mode. Both from Li et al. [58].*

Jokela *et al.* [59] have provided a thorough investigation of N-H complexes in ZnO by means of FTIR spectroscopy combined with isotope exchange methods. Polycrystalline ZnO was grown by chemical vapor transport with graphite as a transport agent. The reaction was performed in a silica ampoule containing 0.5 atm NH_3(g), N_2(g) or Ar(g). FTIR analysis showed a peak at 3150.6 cm^{-1} only for the sample prepared in ammonia. This peak was unambiguously assigned to N-H complexes

[6]SIMS uses a primary ion beam to sputter a specimen which generates a secondary ion beam that is analyzed with a MS.

by isotope exchange with both deuterium gas and $^{15}NH_3$ (figure 3.9). Furthermore, the peak only emerged with anhydrous ammonia or Zn-rich conditions, which was found to be consistent with the complexes to reside on oxygen sites.

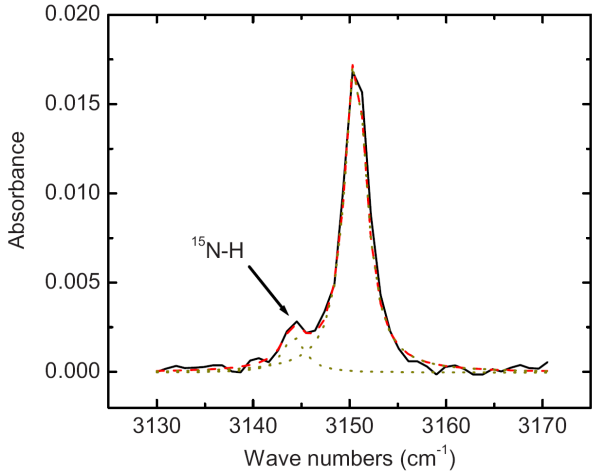

Figure 3.9: *IR spectrum of N-H complexes in ZnO grown in isotopically enriched ammonia (10 % $^{15}NH_3$ + 90 % $^{14}NH_3$). The ^{15}N-H absorption peak, indicated by the arrow, is shifted towards higher frequency as expected for a heavier element. From Jokela et al. [59]*

The stability of the N-H complex was investigated through an annealing series for 1 h in air, and it was found that the N-H complex dissociated in the temperature range between 600–800 °C.

Lu *et al.* [60] have investigated the role of hydrogen in nitrogen doped ZnO thin films prepared with hydrogen in the growth environment. The films were treated in a rapid thermal annealing system in inert atmosphere for 5 min at temperatures from 425–600 °C. Figure 3.10 shows variations in nitrogen and hydrogen concentrations in SIMS depth profiles obtained after annealing at 500 and 600 °C compared to an as-grown film. After the 500 °C anneal, there was observed a significant reduction in the concentration of hydrogen while that of nitrogen remained constant. Hall-effect measurements confirmed these films to be *p*-type. This was explained by dissociation of the N-H complex and out-diffusion of hydrogen which leaves nitrogen to behave as an effective acceptor, N'_O.

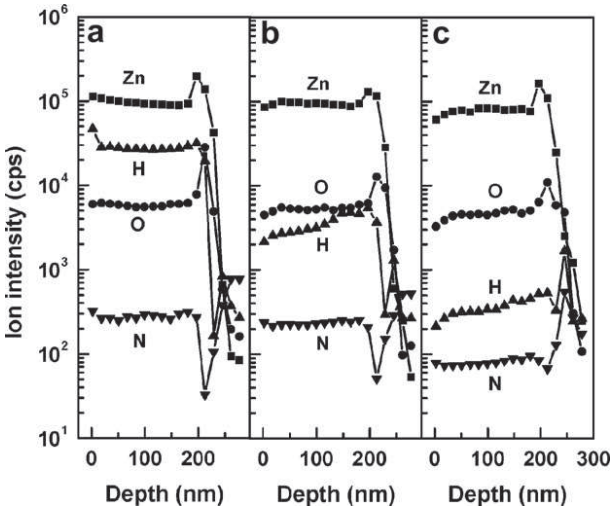

Figure 3.10: *SIMS depth profiles showing variations in hydrogen and nitrogen concentrations after annealing at b) 500 °C and c) 600 °C compared to the as-grown film. From Lu et al. [60].*

As out-diffusion of nitrogen occurred at 600 °C (figure 3.10), films of *p*-type character were obtained only with annealing in a narrow temperature range between 475–500 °C.

In a follow up article by the same group [61], the *p*-type conductivity is stated to be unstable and could be maintained for only 10 days. The reason for this instability of the electrical character of nitrogen doped ZnO is still under debate.

Diwald *et al.* [62] proposed the existence of N-H complexes in rutile TiO_2 based on XPS analysis of single crystals treated in flowing ammonia for 5 min at 600 °C. XPS measurements revealed, in addition to the nitride peak at 396.7 eV, a new peak at higher binding energy, 399.6 eV, in the bulk of the crystal after 60 nm Ar^+ sputtering. This peak is attributed to a nitrogen species carrying less negative charge than the nitride ion, and the binding energy was found to correspond well with other XPS data on NH_x[7] containing compounds. By comparison, only the nitride peak was observed in previous experiments with nitrogen implanted samples by the same group [63].

[7] NH_x: x refers to the number of hydrogen atoms and not a crystallographic site.

Furthermore, the authors propose that the presence of hydrogen as acceptor passivation in the N-H complex increases nitrogen solubility by analogy with the co-doping method proposed by Yamamoto [64]. According to the co-doping model, increased solubility of nitrogen is attributed to an electrostatic energy gain associated with partial compensation of the acceptor by donors.

N-H complexes have been identified by FTIR also in ZnSe prepared by chemical vapor deposition [65], which further supports N-H complexes as a significant nitrogen related defect also in compounds other than oxides.

3.5 Conductivity and transport properties

3.5.1 Conductivity of N-doped ZrO_2 and YSZ

Wendel *et al.* [66] investigated the effect of nitrogen incorporation into YSZ on the electrical conductivity. Samples of YSZ were nitrided with N_2 gas at 1600–1900 °C for 2–4 h in a graphite heated resistance furnace. The electrical conductivity of the nitrided samples was measured in vacuum (10^{-19} bar) by impedance spectroscopy and the nitrogen content was determined by hot gas extraction. Figure 3.11 shows how the conductivity varies with nitrogen concentration in samples doped with 8 and 16 cation % Y.

For the 8 cation % doped sample, an increase in conductivity with nitrogen concentration was observed (figure 3.11(a)). This is explained by an increase in the number of oxygen vacancies due to the nitrogen acceptors. On the other hand, for the 16 cation % doped sample (figure 3.11(b)), the conductivity is lowered with addition of nitrogen.

Under isothermal conditions, a conductivity maximum is observed for a total vacancy concentration of approximately 4 %, independent of the ratio between Y and N acceptors. Thus, it is concluded that the ionic conductivity is affected by Y and N acceptors in a nearly identical way. However, the activation energy for conduction was found to differ between the purely Y-doped and similarly Y/N co-doped samples, where a higher activation energy was observed for the latter. Based on work

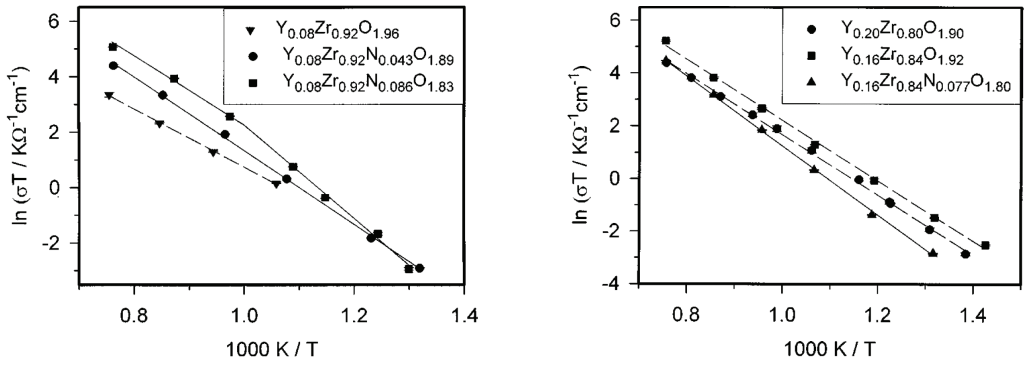

(a) (b)

Figure 3.11: *Arrhenius plots for bulk conductivity of nitrogen doped YSZ in comparison with nitrogen-free reference samples. a) 8 cation % doped and b) 16 and 20 cation % doped samples.*

with other cation dopants, the authors suggest that these variations in the activation energy originates from different binding energies between the dopants and the charge carrier, $v_O^{\bullet\bullet}$.

In this respect, Lee *et al.* [67] have provided a thorough comparison between cation and N-doped zirconia with focus on defect–defect interactions. Based on earlier studies on the structure and conductivity of these systems, the authors conclude that size-matched dopants exhibit superior high temperature conductivity due to low dopant–vacancy interactions. However, as a vacancy ordering process, which occurs at low temperatures, is consequently favorable for these dopants, the low temperature conductivity is deteriorated. Thus, above the vacancy order–disorder transition, conductivity increases with doping (up to 4 % vacancies), and below this transition temperature, conductivity decreases with dopant concentration due to strong defect interactions.

3.5.2 Electrical properties of TiO_xN_y thin films

Martin *et al.* [68] have investigated the electrical properties of titanium oxynitride thin films deposited by a reactive magnetron sputtering technique from a Ti-target and $Ar/N_2/O_2$ gas mixtures. The oxygen and nitrogen content of the films were determined by electron probe

microanalysis (EPMA) with wavelength dispersive spectroscopy (WDS). Films of TiO_xN_y with the cubic TiO—TiN structure had compositions between $TiO_{0.82}N_{0.63}$ and $TiO_{1.02}N_{0.57}$, and thus included a considerable amount of non-stoichiometry. Figure 3.12 shows the conductivity of the films as measured by the van der Pauw method. The electrical conductivity is said to follow an exponential behaviour with an activation energy of 39 to 70 meV for the cubic oxynitrides.

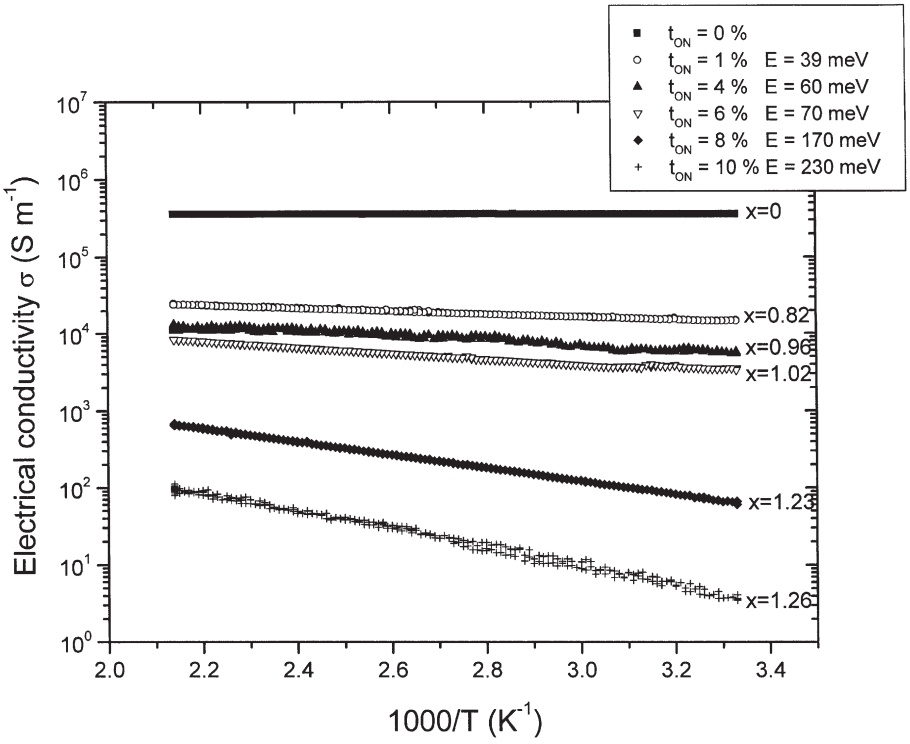

Figure 3.12: *Conductivity data of TiN_xO_y thin films. x=0.82, 0.96 and 1.02 are solid solutions of TiO and TiN. From Martin et al. [68]*

Chapter 4

Experimental

4.1 Materials and sample preparation

Table 4.1 lists the compounds and corresponding sintering conditions for the samples that were investigated. In some cases, multiple samples were prepared of the same material with variations in sintering conditions and density. If not specifically noted, results are based on a sample of same relative density as in the table. Source material for the RE_6WO_{12} samples was prepared by Anna Magrasó i Solà[1] through a wet chemical synthesis with a 2 h calcination at 600 °C and 700 °C for RE = Sm and Gd, respectively. The resulting nanopowder was calcined again at 1000 °C for 2 h before sintering. All powders were uniaxially cold pressed to disc samples ($\varnothing = 25$ mm) at a pressure of approximately 100 MPa. After sintering, they were analyzed for phase purity by XRD. The binary oxides were all single phase, while the tungstates showed some segregation of RE_2O_3. In a recent study by Magrasó *et al.* [69], single phase lanthanum tungstate is obtained for La/W ratios between 5.3 and 5.7. Also here, segregation of RE_2O_3 was observed for higher La/W ratios.

The diffusivity of nitrogen in oxides is generally much lower than that of oxygen *e.g.* 10^4 times slower in YSZ [70]. From a statistical point of view, this can be explained by the need for two defects, N'_O and $v^{\bullet\bullet}_O$, to be adjacent to one another for nitrogen to diffuse, while oxygen

[1] FERMiO, University of Oslo, Norway.

diffusion occurs by vacancies alone. Hence, sintering conditions were chosen to obtain porous samples ensuring increased surface area and reduced diffusion lengths needed for equilibration. This way, samples can equilibrate in nitriding atmospheres within a time frame suitable for experiments.

Table 4.1: *Sample preparation: sintering conditions (sintering temperature, dwell time, ramp rate), relative density and starting material.* $3YSZ = Zr_{0.942}Y_{0.058}O_{1.971}$. $8YSZ = Zr_{0.852}Y_{0.148}O_{1.926}$. *The 8YSZ specimen was used only for surface analysis with XPS.*

Compound	**Sintering**			**Density**	**Powder**
	°C	hours	°C/h		
TiO_2	850	5	250	∼ 65 %	99.9 % (Aldrich)
ZnO	800	3	180	∼ 83 %	*zur analyse* (Merck)
ZrO_2	1260	2	180	∼ 70 %	99 % (Aldrich)
3YSZ	1260	2	180	∼ 80 %	TZ–3Y (TOSOH)
8YSZ	1500	5	180	∼ 98 %	TZ–8Y (TOSOH)
Nd_2O_3	1300	2	200	∼ 70 %	99.9 % (Molycorp)
Gd_2O_3	1300	2	200	∼ 64 %	99.99 % (Molycorp)
Er_2O_3	1600	2	200	∼ 63 %	98 % (Molycorp)
Y_2O_3	1500	2	180	∼ 61 %	High Purity (Megon)
Sm_6WO_{12}	1500	2	250	∼ 70 %	*see text*
Gd_6WO_{12}	1550	2	250	∼ 60 %	

4.2 Characterization methods

4.2.1 X-ray diffraction — XRD

XRD was used to identify the crystal structure and phase purity of the sintered samples, but also to investigate possible phase transitions and

other structural effects as a result of nitrogen incorporation.

All XRD experiments were carried out with a D 5000 (Siemens) diffractometer using Bragg-Brentano geometry in a θ–2θ setup. The X-Ray source consists of an X-ray tube with a Cu-target producing the characteristic Cu $K_{\alpha 1}$ and Cu $K_{\alpha 2}$ X-rays. A monochromatic beam of Cu $K_{\alpha 1}$ ($\lambda = 0.1541$ nm) X-rays was obtained with a primary monochromator. The instrument is equipped with a position sensitive solid state detector (Braun) and a variable slit.

The raw data was processed with EVA 8.0 (Bruker–AXS) and compared with patterns from the PDF database distributed by ICDD[2]. In some cases, a more detailed data analysis was performed with the FullProf software package [71]. Through the use of *Le Bail* profile matching, lattice parameters could be extracted from the diffractograms.

4.2.2 Scanning electron microscopy — SEM

A Quanta 200F (FEI) with a field emission gun was utilized for surface micrographs. Phase contrast and topographic details are obtained with a solid state back-scattered electron detector and an Everhardt-Thornley secondary electron detector, respectively. Furthermore, the instrument is capable of operating in low vacuum and under humid conditions which enables imaging of poor conductors without any further sample preparation.

The instrument is also equipped with an energy dispersive spectroscopy (EDS) system (EDAX) for quantitative elemental analysis. However, the spectral resolution is not high enough to separate light elements such as nitrogen and oxygen.

4.2.3 X-Ray photoelectron spectroscopy — XPS

Out of the characterization methods used in this work, XPS is the only one capable of direct elemental analysis of nitrogen in an oxide structure. Furthermore, in addition to being a quantitative method, information on

[2]PDF = Powder Diffraction File, ICDD = International Centre for Diffraction Data.

the electronic state of the specimens constituents can be extracted from the spectra.

In addition to a survey scan, detailed scans of the C 1s, O 1s, N 1s and the main cation peak were recorded. The N *KLL* auger peak is of lower intensity than the 1s peak and was not prioritized for detailed scans. Charging of the samples was compensated by a positive current of Ar^+ ions which causes a shift of the whole spectrum. The C 1s peak was then used as a reference by aligning it to the default value of 285 eV. Data analysis was performed with CasaXPS (Casa Software Ltd).

The instrument, AXIS Ultra^{DLD} (Kratos), features Al, Ag and Mg anodes wherof monochromatic Al $K_{\alpha 1}$ (1486.6 eV) and achromatic Mg K_α (1353.6 eV) X-rays were utilized.

4.2.4 Mass spectrometry — MS

A mass spectrometer was used for gas phase analysis (GPA) during degasification experiments in which a sample is heated in vacuum and gases that are released can be quantified. The setup, shown in figure 4.1, consists of a Prisma QME 200 quadrupole MS (Pfeiffer) and a tube furnace. The MS is equipped with both a Faraday and C-SEM detector, but only the latter was used due to its lower detection limit of down to 10^{-14} mbar.

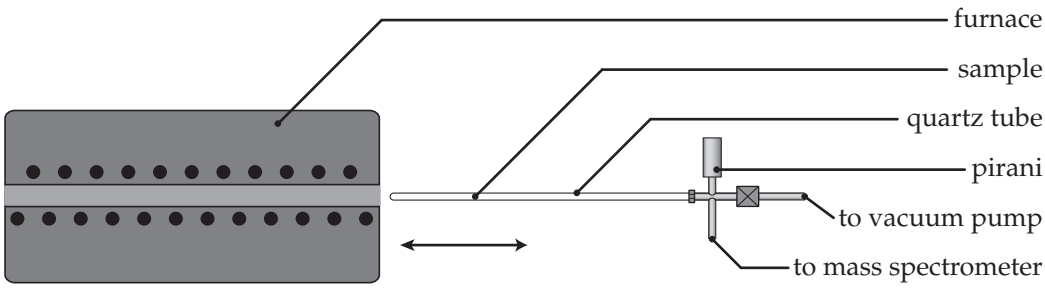

Figure 4.1: *Setup for degassing experiments. The specimen is loaded in a quartz tube, and can be instantaneously exposed to high temperatures by inserting the tube into the furnace. The chamber pressure was measured with a pirani gauge.*

Table 4.2: *Mass number for fragmented ions above 2 % of the base peak. The mass numbers are listed in order of decreasing concentration. The sensitivity factors are for the base peak, and this is not listed for ammonia [72].*

Gas	**Mass number**	**Sensitivity factor** $[\times 10^{-5}\,\mathrm{A/mbar}]$
H_2	2	13
NH_3	17 16	—
H_2O	18 17 16	20
N_2	28 14	20
O_2	32 16	14

The mass numbers[3] that were measured are shown in table 4.2. Uncertainties due to mass number overlap between different species was avoided by measuring multiple mass numbers for each gas. A constant ratio between the signal of these mass numbers then gives a clear indication of which gas that is measured. Similarly, leakage of air can be disregarded when there is no correlation between the intensities of the oxygen and nitrogen mass numbers during the experiment.

Quantification was done by relating the total pressure in the sample chamber with the relative concentrations of gases as measured by the MS at room temperature prior to degassing. It is then assumed that no other gases than those measured contribute significantly to the total pressure. The reliability of this procedure was tested with a 10 % H_2 10 % He 80 % N_2 calibration gas (Hydro). The intensity of the mass number for hydrogen showed large variations (in the order of one magnitude) for different pressures in the MS analysis chamber[4] Thus, hydrogen intensities are accompanied by large uncertainties which also affect the relative intensities of the other species.

[3]Mass number refers to mass/charge ratio.

[4]In the GPA-MS setup, gas analysis is done by injecting a small amount of gas from the sample chamber into the MS. The pressure inside the MS is regulated by a needle valve.

4.2.5 Fourier transformed infrared spectroscopy — FTIR

Identification of N-H complexes was attempted for yttria and zinc oxide samples by means of FTIR in the same manner as described in section 3.4.3 of the literature review. Specimens were prepared by embedding powder from ammonia treated disc samples in a solid KBr matrix (IR-quality, Merck). Due to the hygroscopicity of KBr, and the overlap of the O-H stretch in water and the reported N-H stretch frequency, the specimens were stored in a P_2O_5 exicator. The transmittance was very low in the region of interest ($2800-3500\,cm^{-1}$) for all samples. Combined with the low absorbance reported for the N-H stretch in ZnO [58, 59], no valuable information could be extracted from the spectra. The FTIR data will therefore not be further discussed.

The instrument was a IFS 66v/S (Bruker) equipped with a DTGS[5] detector capable of a spectral resolution of $2\,cm^{-1}$. Transmittance spectra were recorded in vacuum at room temperature.

4.3 Apparatus

4.3.1 Measurement cell

A ProboStat (NorECs) measurement cell was used for the electrical characterization of the disc samples allowing high temperatures and a gas tight environment. The cell, shown in figure 4.2, contains an inner alumina tube on which the sample rests. Four platinum electrode wires were attached to two alumina rods and pressed on top of the sample with a spring load, ensuring good contact between the electrodes and the sample. The electrodes were arranged in an approximately square geometry towards the edges of the sample. The gas from the inner and outer inlets was led directly to the vicinity of the sample by alumina tubes. The gas outlets are situated at the base of the tube assuring good circulation of gas. A Pt/Pt-10%Rh thermocouple (S-element) was fitted close to the sample for temperature measurement.

[5] Deuterated triglycine sulfate.

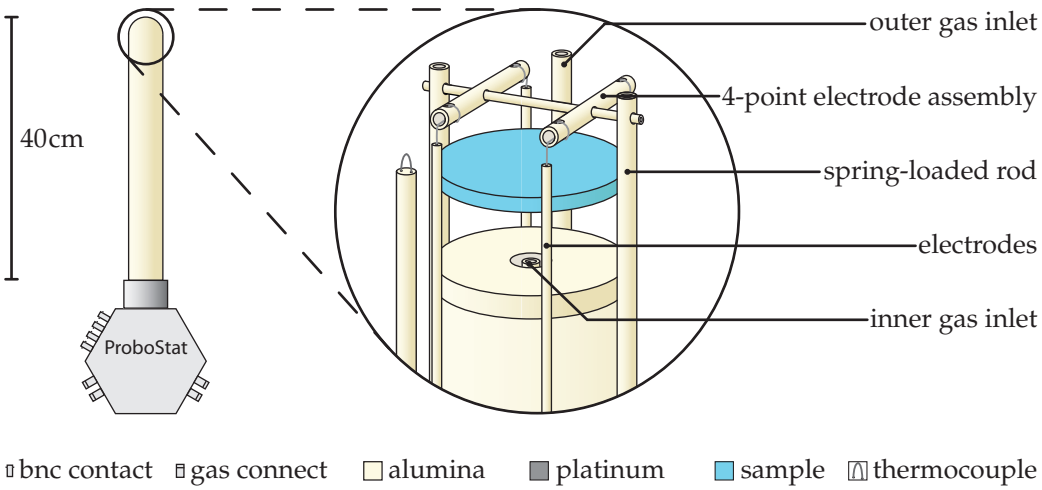

Figure 4.2: *ProboStat measurement cell with detailed view of a sample mounted with four electrodes in a van der Pauw configuration.*

The outer alumina tube protects the system and makes the outer chamber gas tight towards the surrounding atmosphere. The length of the inner tube serves to distance the hexagon base, containing heat sensitive electronic wiring and polymer gaskets, from the high temperature region. All the inner metal parts of the cell were made of stainless steel in order to withstand the corrosive nature of ammonia. The hot-zone of the cell was inserted into a vertically mounted resistance furnace capable of operating at temperatures up to 1250 °C.

4.3.2 Gas mixer

Controlled atmosphere in the measurement cell were obtained with a gas mixer. The setup used for all experiments with ammonia is shown in figure 4.3.

The gas mixer is based upon three ShoRate 1355 flowmeters: A, B and C. The ammonia flow was adjusted with a 18–turn needle valve directly on the gas bottle and the flow was read from flowmeter A. Flowmeter B

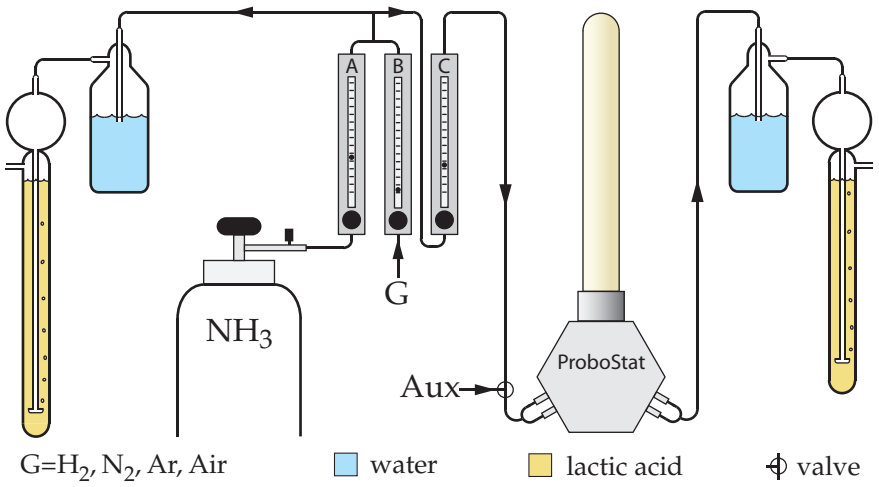

Figure 4.3: *Gas mixer for ammonia with an auxiliary input (aux).*

could be used to dilute the ammonia from A, or to run pure H_2, N_2, Ar or air. Flowmeter C controls the flow of gas to the cell and was calibrated for ammonia (appendix A). The excess gas from A + B (Mix1) and the gas from the cell outlet was led through ammonia traps (described below). These columns provide the pressure gradient necessary to drive gas through the cell. In addition, the overpressure in the system reduces the amount of gaseous impurities from the surrounding atmosphere. All metal parts leading ammonia were made of stainless steel.

As shown in the figure, the setup was built with an input for an auxiliary gas mixer. This was used when wet and diluted gases other than ammonia was necessary *e.g.* for p_{O_2}, p_{H_2} and p_{H_2O} dependencies. A more advanced gas mixer with these capabilities is described and illustrated in appendix B. The auxiliary input provided instantaneous switching between the mixers during experiments without the need to open the system and expose the sample to an oxidizing environment.

During experiments, a continuous flow of gas was flushed through the cell, limiting the effect of leakages and removing reaction products such as water. In the case of ammonia gas the flow rate is an important parameter because of the kinetically limited decomposition reaction at elevated temperatures. For the same reason, the partial pressure of

ammonia in the cell is not defined by gas phase equilibria. Thus p_{NH_3} dependencies on the conductivity could not be carried out with the current setup. Furthermore, at the extremity of dry and reducing gas at high temperature, p_{O_2} is largely dependent on the impurity levels of water and oxygen through the equilibrium

$$H_2O(g) \rightleftharpoons H_2(g) + \tfrac{1}{2}O_2(g) \tag{4.1}$$

The impurity level of oxygen is estimated to 1×10^{-5} bar based on the purity of the supply gas, and that of water to 3×10^{-5} bar as estimated by Norby and Kofstad [73] for a similar apparatus. Because these these values are associated with considerable uncertainties, p_{O_2} was not always well defined under the experimental conditions that were employed.

Ammonia trap

Ammonia gas is poisonous and corrosive and therefore needs to be neutralized prior to disposal. This was done by leading the excess gas from the gas mixer and the gas that had passed through the cell, through bubblers containing lactic acid. Ammonia reacts with lactic acid to form an ammonium lactate by the following reaction

$$NH_3(g) + C_3H_6O_3(l) \rightarrow NH_4C_3H_5O_3(l) \tag{4.2}$$

An increased reaction surface was achieved with gas dispersion filters in the lactic acid columns. As shown in figure 4.3, the gas was passed through water before entering the bubbler containing lactic acid. The water bubbler served as a buffer and to prevent ammonia gas from being in direct contact with the lactic acid. A wetted litmus paper placed at the bubbler outlet proved to be an effective way of detecting ammonia. This method was used to determine when the lactic acid was saturated and needed to be exchanged.

Detection of ammonia

A simple qualitative test was used to verify that not *all* the ammonia gas was decomposed under the experimental conditions. The gas from the cell

was bubbled through a 30 mL 0.1 M HCl solution with a phenolphthalein pH indicator. When ammonia was present in the gas, it neutralized the acid and triggered a change in color when the pH of the solution exceeded 8.0–9.6 [74].

Unfortunately, too many variables prevented the use of this method for even a semi-quantitative estimation of the partial pressure of ammonia in the hot zone of the cell. These are mainly associated with a non-uniform color change, uncertainty regarding decomposition of ammonia on the way out of the cell and possibly the reaction rate of the gas with the acidic solution.

4.3.3 Electrical measurements

In the present work, conductivity measurements is the main method of characterization. The measurements were performed with the van der Pauw 4–point method (section 2.3) in controlled atmospheres using the ProboStat measurement cell (section 4.3.1). These measurements were carried out to probe effects of nitrogen incorporation with respect to alteration of the concentration and mobility of charge carriers according to equation 2.9. Furthermore, such measurements will in most cases give indications of structural and compositional changes in the sample. The basic starting point for material characterization was a comparison of the conductivity in anhydrous NH_3 and a dry H_2/Ar mixture of similar p_{O_2}.

Conductivity was measured with a SI-1260 Impedance/Phase–Gain analyzer (Solartron) by applying a 1 V (rms) oscillation voltage at 1592 Hz. The van der Pauw switching was done automatically by a multiplexer (Pickering).

Due to the low porosity of the samples, the measured conductivity values were compensated by an empirical factor [75]

$$\sigma_{real} = \frac{\sigma_{measured}}{\rho^2_{relative}} \tag{4.3}$$

where σ is conductivity and $\rho_{relative}$ is the relative density of the sample (table 4.1).

Due to the high resistivity of undoped RE_2O_3 compounds, the temperature range where these samples could be characterized was limited by the instrumental setup to typically $>1000\,^{\circ}C$ for the van der Pauw method to give reliable results.

High temperature combined with reducing conditions had a detrimental effect on the platinum electrodes, making them fragile. Furthermore, platinum showed a tendency to wet the sample surface or even sink into the more porous samples under these conditions. This was most pronounced for long treatments in ammonia. In this respect, the errors associated with the van der Pauw method related to electrode area and placement are addressed in the following section. Gold electrodes were avoided due to their limitation in temperature *i.e.* melting point: $1064\,^{\circ}C$.

A 2–point electrode setup was briefly used, but the porous platinum electrode (paint + grid) proved to be too catalytic towards ammonia decomposition. In contrast to the van der Pauw point electrodes, these electrodes cover the sample surface on both sides so that the gas has to pass through the electrode in order to reach the sample.

4.4 Sources of error

Conductivity

In order to estimate the order of magnitude of the error introduced by non-ideal electrode area and placement, van der Pauw [15] derived an approximation formula for some special cases. It is assumed that the contacts are placed at angles of $90\,^{\circ}$ on a circular disc sample, and that the area of the contact is an equipotential area. The relative error, $\frac{\Delta\rho}{\rho}$, for one contact of width $d_{\parallel}$ along the circumference is then given by

$$\frac{\Delta\rho}{\rho} = -\frac{d_{\parallel}^2}{16D^2 \ln 2} \tag{4.4}$$

where D is the diameter of the sample, ρ is resistivity and the other contacts are infinitely small and located at the circumference.

For an electrode of width $d_\perp$ towards the center of the sample, the relative error becomes

$$\frac{\Delta\rho}{\rho} = -\frac{d_\perp^2}{4D^2 \ln 2} \tag{4.5}$$

And finally, for a point electrode at a distance d from the circumference of the sample

$$\frac{\Delta\rho}{\rho} = -\frac{d^2}{2D^2 \ln 2} \tag{4.6}$$

Moreover, if more contacts exhibit some of the above mentioned attributes, these are to a first approximation additive. The maximum relative error for a typical sample with non-ideal contacts ($d_\parallel = 2\,\text{mm}$, $d_\perp = 3\,\text{mm}$, $d = 1\,\text{mm}$ and $D = 22\,\text{mm}$) then amounts to -0.036 for four electrodes. In addition, as mentioned in section 4.3.3 and 2.3, porosity and unevenness in the thickness of the sample also contribute to uncertainty regarding the absolute conductivity values. Anyhow, variations in the contact resistance of one or more electrodes proved to have a larger influence on the conductivity. This occurred between different sets of electrodes, but also during measurements. The relatively high noise level of the conductivity which can be seen in some of the results is also attributed the electrodes.

XRD

Errors associated with lattice parameters from *Le Bail* fitting were found to depend on the zero-point parameter *i.e.* shift of the spectrum along the 2–θ axis. This value was kept below 0.05 by repeating the diffraction experiment with a more carefully prepared sample.

Chapter 5

Results

Conductivity measurements of the rare-earth oxides, zirconia and the tungstates revealed a temporary effect of ammonia, not in ammonia atmosphere, but while flushing the system with inert gas after ammonia treatment. This was most pronounced for Y_2O_3 and Gd_2O_3 and will be presented in section 5.1.1. The reason for this effect is not yet clear and is therefore left to the discussion in chapter 6. Results involving phase transitions into nitrides and oxynitrides are discussed in conjunction with their presentation in the present chapter. The results are presented individually for each compound or material system except for those from XPS analysis.

5.1 Rare-earth sesquioxides — RE_2O_3

5.1.1 Y_2O_3 & Gd_2O_3

Samples of Y_2O_3 and Gd_2O_3 were electrically characterized at 1000–1200 °C and 1100–1200 °C, respectively. Figure 5.1 shows the conductivity of Y_2O_3 at 1200 °C upon introduction of ammonia. The conductivity equilibrates in the same manner as in H_2 and to a similar, but slightly lower level. Therefore, since Y_2O_3 is an *n*-type conductor under reducing conditions (section 3.1.1), it is reasonable that the conductivity in ammonia is purely an effect of p_{O_2} rather than a nitridation reaction. However, when

ammonia is replaced by an inert gas, conductivity increases abruptly by approximately one order of magnitude. After the maximum is reached, the conductivity slowly deteriorates to the level prior to the ammonia treatment.

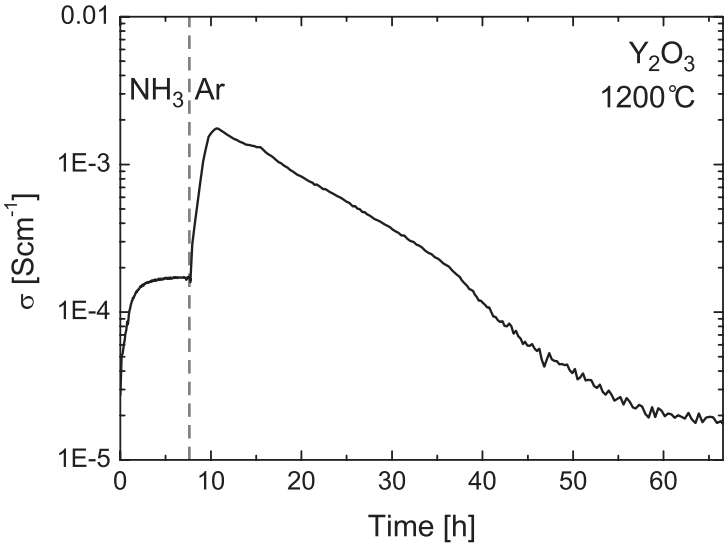

Figure 5.1: *Conductivity of Y_2O_3 at 1200 °C. The gas was changed from Ar to NH_3 at t = 0, and back to Ar at t = 7.5 h. NH_3 flow rate ∼ 20 mL/min.*

Similar experiments are shown for lower temperatures in figure 5.2(a), where it is seen that no such drastic effect occurs below 1200 °C for Y_2O_3. In this figure, the immediate decrease in conductivity upon NH_3/Ar switch at 1000 °C is representative also for similar experiments with H_2/N_2 mixtures or pure hydrogen instead of ammonia.

Furthermore, when air was introduced at the conductivity peak[1], there was an abrupt decrease in conductivity to the level representative for this p_{O_2}. A similar behaviour was observed also with H_2. However, as shown in figure 5.2(b), when hydrogen was replaced by argon, the conductivity increased again in the same manner as before. Furthermore, the effect of ammonia was retained when the sample was quenched[2] in ammonia and heated to 1200 °C in argon (figure 5.3).

[1]The term "conductivity peak" will be used to denote the abrupt increase in

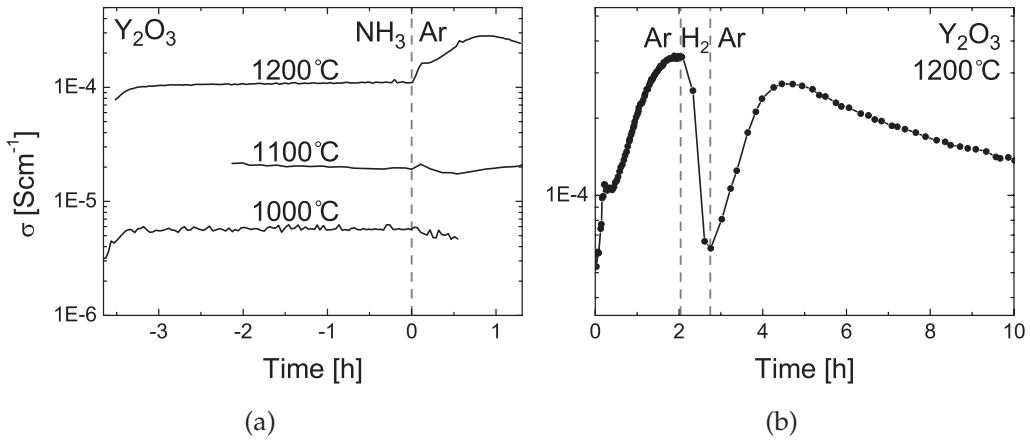

Figure 5.2: *Conductivity isotherms of Y_2O_3. a) Conductivity jump at different temperatures. Ammonolysis time is indicated by the length of the curve before $t = 0$. b) Effect of introducing H_2 at the conductivity peak. The gas was changed from NH_3 to Ar at $t = 0$ and to H_2 for a short time period as indicated.*

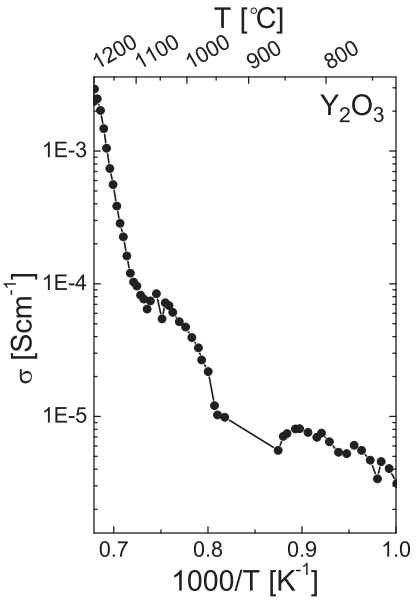

Figure 5.3: *Temperature ramp (78°C/h) from RT to 1200°C in argon. The sample was quenched to RT after a 7.5 h treatment in ammonia at 1200°C prior to this ramp. Due to the relatively fast heating rate, these values are not considered to be at equilibrium.*

conductivity observed upon replacing NH_3 with Ar.

[2]Quenching rates were >450°C/h for the first 500 °C when quenched from above 1000 °C.

As will become clear during the following parts of this chapter, these effects of ammonia were observed also for other oxides, but all aspects were not investigated in every case.

Figure 5.4 shows the similarly pronounced effect of ammonia on the conductivity of Gd_2O_3. In contrast to Y_2O_3, this includes also 1100°C. The magnitude of the conductivity peak was investigated as a function of equilibration time in ammonia and the ammonia flow rate as shown in figure 5.5. From these measurements, it is clear that the flow rate, which translates to p_{NH_3} (section 2.4), has a larger effect than the equilibration time in ammonia.

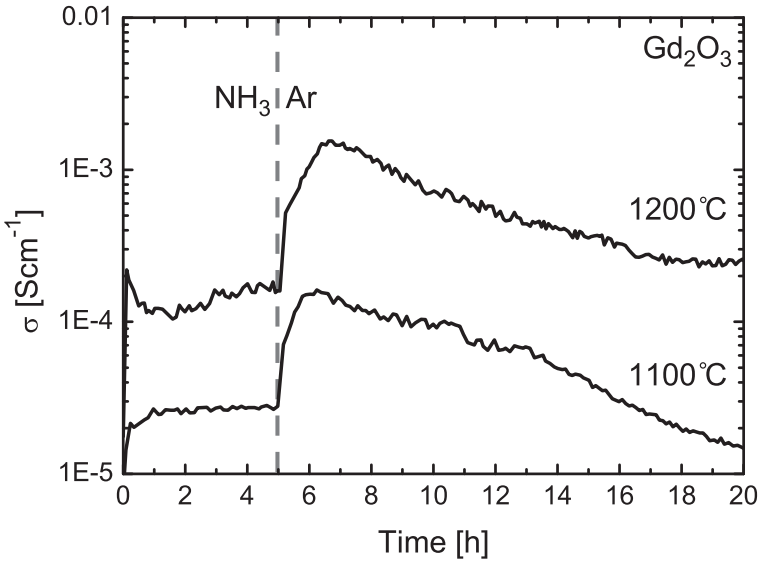

Figure 5.4: *Isothermal conductivity of Gd_2O_3 as a function of time and atmosphere. At $t = 0$, the gas was switched from Ar to NH_3 with a flow rate of 22 mL min^{-1}.*

Although the general trends of these measurements always were repeatable, variations in the absolute value of the conductivity peak and the subsequent decrease in conductivity were observed. Since nitrogen related defects may be substituted by oxygen, it seems reasonable to attribute these variations to different levels of oxygen and water impurities in the system which affect p_{O_2}. Moreover, variations are not unexpected for such a temporary effect under non-equilibrium conditions.

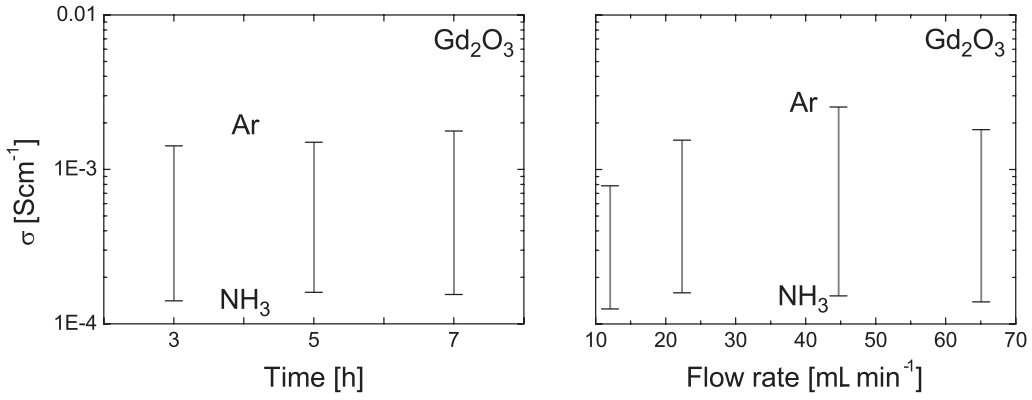

Figure 5.5: *Magnitude of the conductivity peak upon exchanging ammonia with argon for Gd_2O_3 at 1200 °C for a) varying equilibration time in ammonia and constant flow rate of 44 mL min^{-1}, and b) varying ammonia flow rate and 5 h equilibration time. The 3 h and 7 h points were multiplied with a factor of 1.3 and the 22 and 45 mL min^{-1} points with a factor of 1.2 to give comparable results (section 4.4).*

The conductivity obtained at the conductivity peak of Y_2O_3 resembles that of YN at similar temperatures, as reported by Lesunova *et al.* [76]. However, it was verified by XRD that no phase transition had occurred in samples quenched in ammonia and SEM surface micrographs showed no variations in microstructure. Furthermore, oxides of the most electropositive metals, including the rare-earths, are by Elder *et al.* [1] not considered viable as precursors for nitridation with ammonia due to exceptionally unfavorable thermodynamics.

GPA–MS

A degassing experiment of Y_2O_3 was performed at 1100 °C on a sample quenched in ammonia after a 5 h treatment at 1200 °C with flow rate of 44 mL min^{-1}. The sample was first analyzed up to 350 °C to ensure that any release of nitrogen at 1100 °C did not originate from adsorbed ammonia or nitrogen gas. Furthermore, there was no increase in the NH_3 related mass numbers (table 4.2).

Figure 5.6 clearly shows that nitrogen and hydrogen was released from the sample at 1100 °C. This data will be discussed and used further in chapter 6.

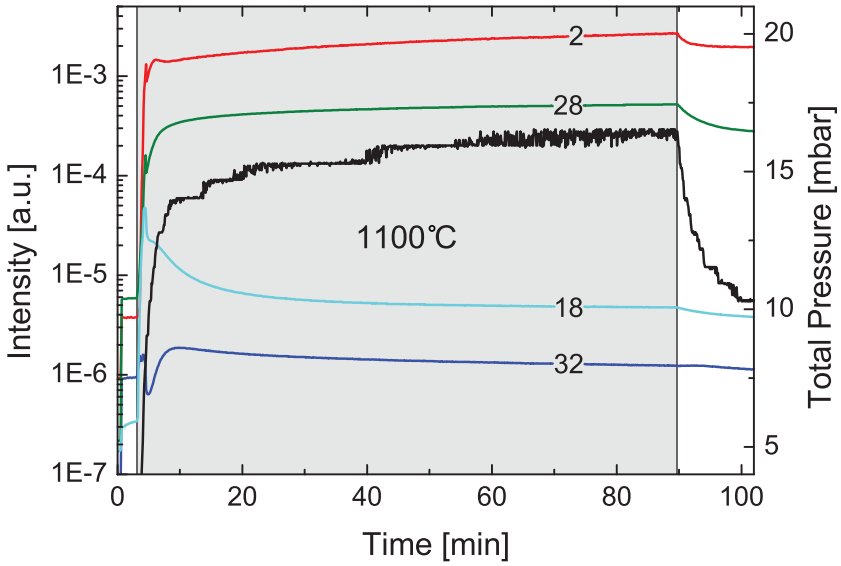

Figure 5.6: *Degassing experiment of a 0.787 g Y_2O_3 sample quenched in ammonia after 5 h at 1200 °C. The intensities for mass number 2 (H_2), 18 (H_2O), 28 (N_2) and 32 (O_2) (left axis) and total pressure (right axis) are shown as a function of time. The grey region represents the interval where the sample chamber was inserted into the furnace.*

5.1.2 Nd_2O_3 & Er_2O_3

In order to survey material specific parameters that could affect the previously described conductivity peak, Nd_2O_3 and Er_2O_3 were briefly investigated in the same manner as Y_2O_3 and Gd_2O_3. Thus, measurements of a selection of sesquioxides along the lanthanide series could be compared. The same characteristics were observed for Nd_2O_3 (figure 5.7(a)) and Er_2O_3 (figure 5.7(b)), although to a somewhat lesser extent than for Y_2O_3 and Gd_2O_3.

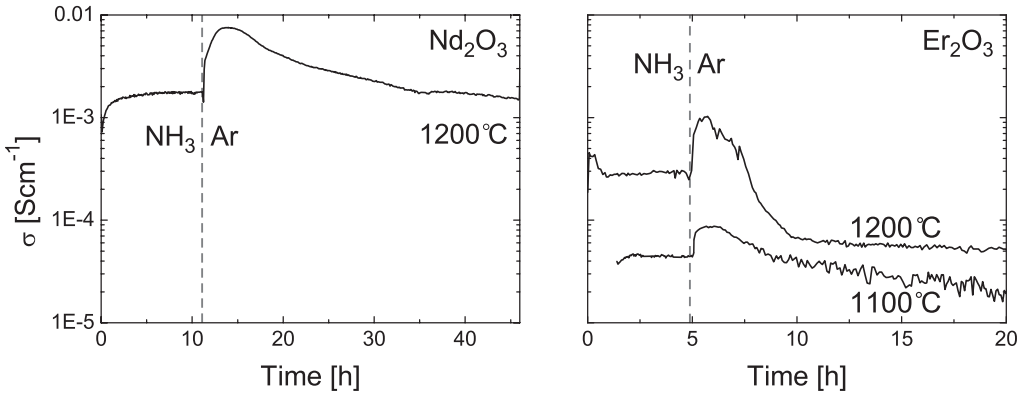

Figure 5.7: *Conductivity of a) Nd_2O_3 b) Er_2O_3 as a function of time and atmosphere. Ar was replaced by NH_3 at $t = 0$ with a flow rate of approximately 20 mL min^{-1}.*

5.2 Zirconia — ZrO_2

Samples of nominally undoped ZrO_2 and 3YSZ were characterized at 1100–1200 °C and 900–1200 °C, respectively. For both samples, a conductivity peak similar to that of the sesquioxides was observed after ammonia treatment (figure 5.8). However, this effect was drastically less pronounced for the doped sample.

Although the conductivity in H_2 was the same as in ammonia for 3YSZ, the conductivity did not decrease to this level upon introduction of H_2 at the conductivity peak (figure 5.8(b)). This represents an interesting difference from the RE_2O_3 compounds where the conductivity peak was completely suppressed in H_2 (figure 5.2(b)). The conductivity peak of the 3YSZ sample at 1100 °C was of similar magnitude to that in figure 5.8(b).

At 1200 °C, ZrO_2 showed an even steeper increase in conductivity in ammonia than at 1100 °C and subsequently a lower conductivity peak in argon. Figure 5.9 shows an X-ray diffractogram after a 3 h treatment in ammonia at 1200 °C which indicates partial transition into $Zr_7O_8N_4$ (section 3.3.1). Furthermore, the sample had cracked and changed color from white to light blue. It is quite probable that formation of $Zr_7O_8N_4$ also occurred at 1100 °C, as indicated by the steady conductivity increase

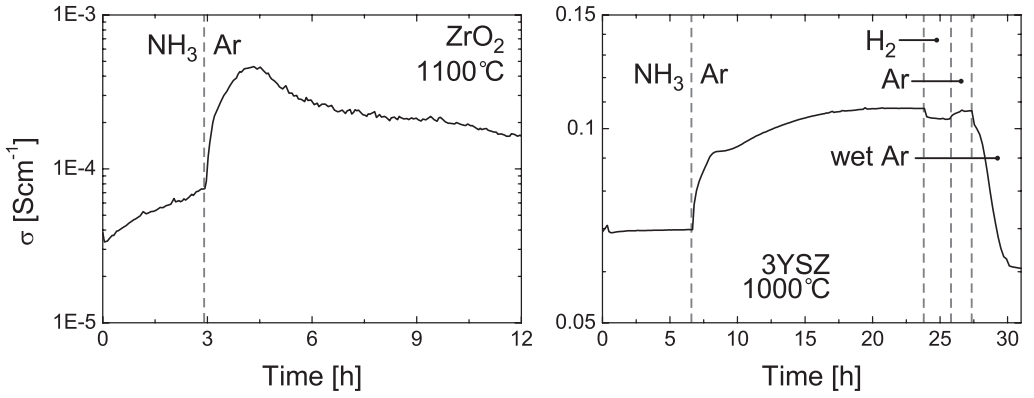

Figure 5.8: *Conductivity of a) ZrO_2 and b) 3YSZ as a function of time and atmosphere. The atmosphere was switched from Ar to NH_3 at $t = 0$.*

during ammonolysis also at this temperature (figure 5.8(a)). It should be noted that the monoclinic–tetragonal phase transition temperature is 1170 °C (section 3.1.3). However, due to the similarities in the conductivity behaviour at 1100 and 1200 °C, it seems that the effect of ammonia is the dominating process also at 1200 °C.

During a 77 h treatment in ammonia at 1200 °C, the 3YSZ sample showed a steady increase in conductivity from 0.1 S cm^{-1} to 0.22 S cm^{-1}. After quenching to RT the sample had clearly started to decompose into a powder, but XRD did not show any new phases. On the other hand, a similar experiment at 1000 °C yielded a black scale on the sample surface, which was determined to contain ZrN by XRD. The formation of ZrN at lower temperature may be explained by the lower p_{O_2} at 1000 °C compared to 1200 °C[3].

[3]Considering a p_{O_2} vs. temperature phase diagram for ZrO_2—ZrN [16].

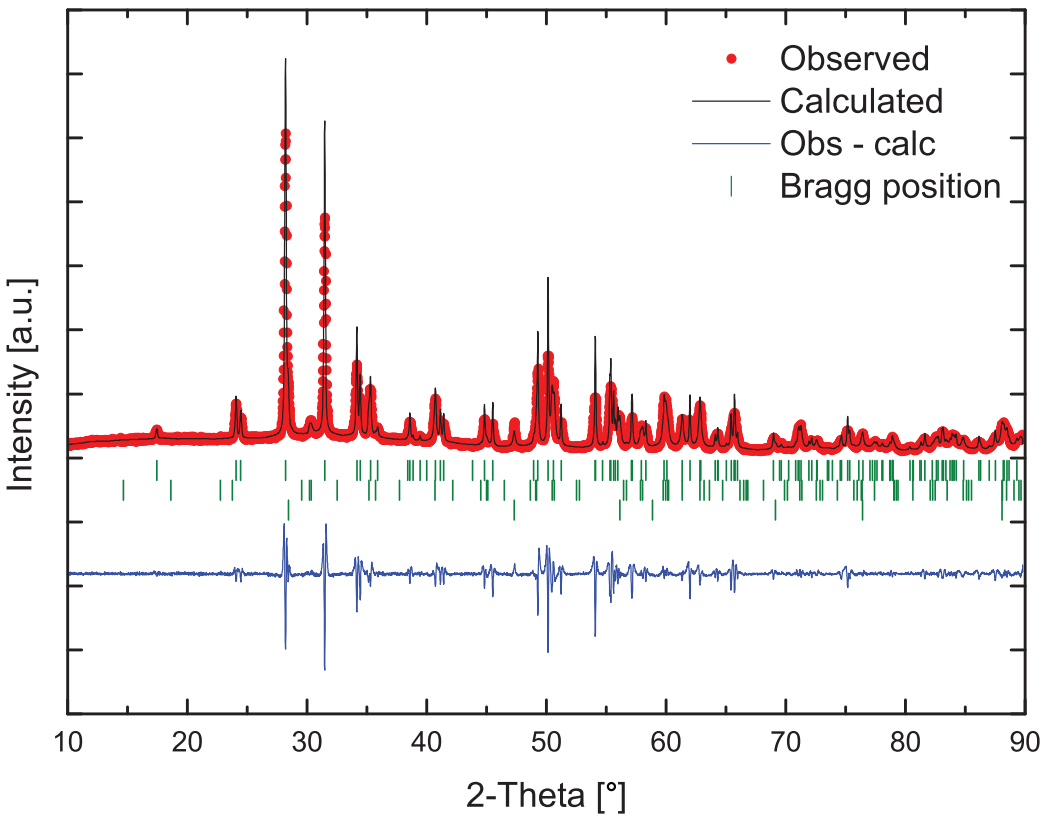

Figure 5.9: *X-ray diffractogram from powder with added silicon standard showing zirconia ($P\,2_1/a$) and the oxynitride phase ($R\,\bar{3}$). Bragg positions refer to ZrO_2 (top), $Zr_7O_8N_4$ (middle) and Si (bottom). $Zr_7O_8N_4$ contains many peaks of low intensity which are not visible due to the low concentration of this phase. However, the main peaks are visible at approximately 30° and as a shoulder at 35°.*

5.3 Rare-earth tungstates — RE_6WO_{12}

5.3.1 Conductivity

As with the ZrO_2 sample, both Sm_6WO_{12} and Gd_6WO_{12} showed indications of a nitridation processes occurring in ammonia atmosphere. Both samples also showed a conductivity peak upon replacing ammonia with argon as previously described. Figure 5.10 shows conductivity isotherms of Gd_6WO_{12} and the conductivity peak in argon for two differ-

ent ammonolysis times. The initial increase in conductivity is attributed to changes in p_{O_2} as ammonia decomposes to give more reducing conditions and increased *n*-type conductivity. After a few hours another process seems to take over that suppresses conductivity. This may be

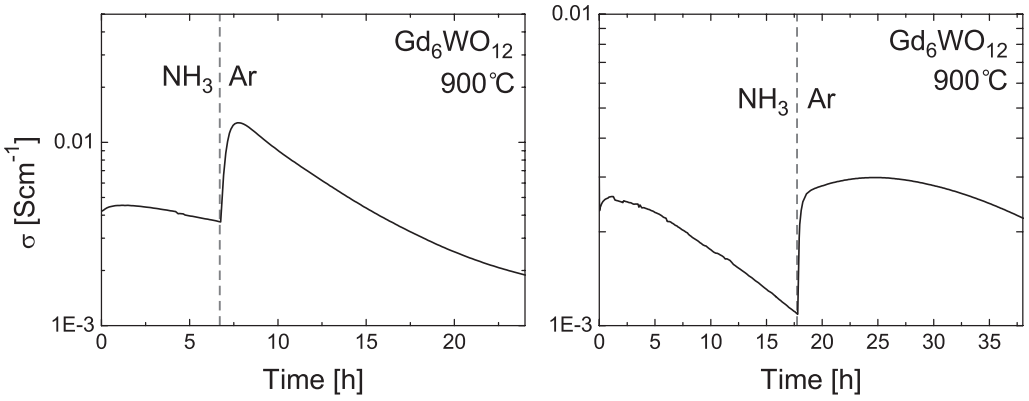

Figure 5.10: *Conductivity of Gd_6WO_{12} as a function of time and atmosphere. Note the different treatment times in these two experiments.*

Figure 5.11 shows a prolonged ammonolysis experiment in which conductivity is drastically increased after the initial decrease. Furthermore, during quenching in ammonia, the conductivity showed a low temperature dependency, and decreased only to $0.8\,\mathrm{S\,cm^{-1}}$ at 300 °C. At this temperature, the sample cracked, and the color had changed from pale yellow to completely black. Diot *et al.* [46] (section 3.3.2) also obtained black powders for the largest rare-earth elements, La and Nd, when nitridiation was carried out above 900 °C and this was attributed to reduction of W(+VI). Furthermore, the reduction phenomenon, which was particularly associated with the highest nitrogen contents, was explained by an incompatibility between the rare-earth cation and a sixfold coordination resulting from the increasing proportion of vacancies.

Thus, the RE = Sm sample was characterized at lower temperatures. At 600 °C there was no distinctive effect of ammonia. However, as shown in figure 5.12, the nitridation process in ammonia and the conductivity peak in argon appeared at higher temperatures.

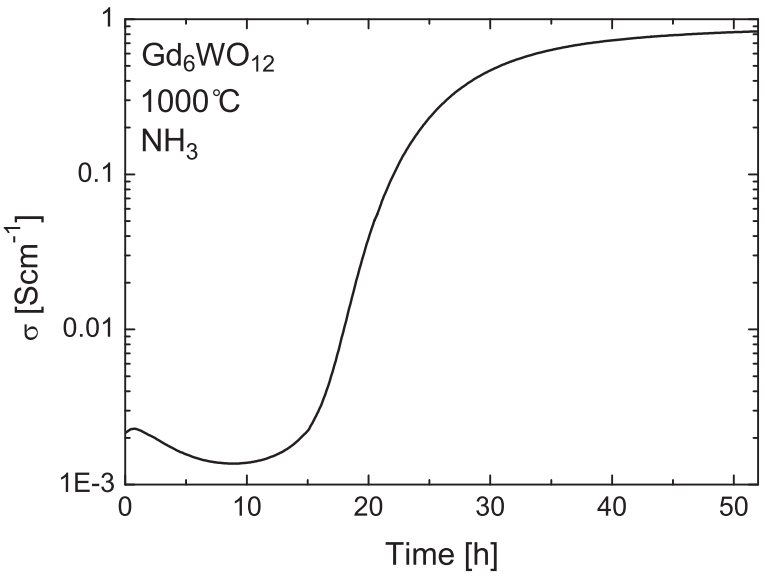

Figure 5.11: *Conductivity of Gd_6WO_{12} in ammonia at 1000 °C.*

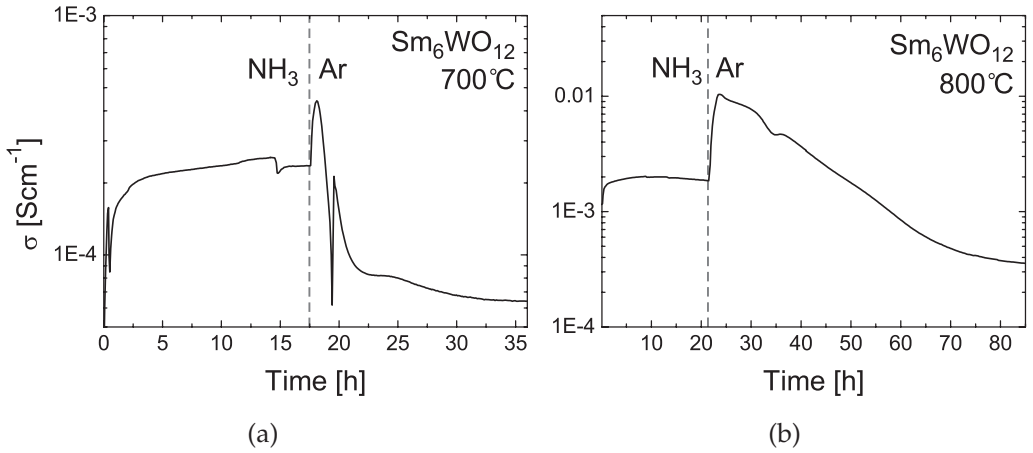

Figure 5.12: *Conductivity of Sm_6WO_{12} as a function of time and atmosphere at a) 700 °C and b) 800 °C. Argon was replaced with ammonia at t = 0. Variation in the conductivity in ammonia at 700 °C was due to a varying flow rate and thus also p_{O_2}.*

5.3.2 XRD

XRD of the Gd_6WO_{12} sample after ammonolysis revealed a severe reduction in crystallinity as indicated by a 70:1 ratio between the intensity

Table 5.1: *Lattice parameters of the reduced Gd_6WO_{12} sample and fully nitrided RE = Ho,Y oxynitrides fitted to the $F\,m\,\bar{3}\,m$ space group. The crystal radii of the rare-earth cations apply for six-fold coordination [2] which is the average coordination in the fully nitrided powders i.e. bixbyite stoichiometry. Refinement parameters: Zero-point = 0.0094 °, $\chi^2 = 1.12$.*

Phase	**Lattice parameter [Å]**	**Rare-earth radius [Å]**
reduced Gd_6WO_{12}-sample	5.39(1)	1.078
$Ho_{3.43}W_{0.57}O_{4.3}N_{1.7}\square_2$	5.2737(6) [46]	1.041
$Y_{3.43}W_{0.57}O_{4.3}N_{1.7}\square_2$	5.2770(4) [46]	1.04

of the main peak for the as-sintered and reduced sample, respectively. Furthermore, the background noise was relatively high even with a silicon single crystal powder sample holder[4]. Figure 5.13 shows the diffractogram of the reduced sample fitted to a $F\,m\,\bar{3}\,m$ space group as proposed, to a first approximation, by Diot *et al.* [46] (section 3.3.2). The lattice parameter, listed in table 5.1, is in qualitative agreement with those reported for the fully nitrided oxynitrides with respect to the size of the rare-earth cation. Thus, it seems that the reduced Gd_6WO_{12}[5] contains the fully nitrided oxynitride, $Gd_{3.43}W_{0.57}O_{4.3}N_{1.7}\square_2$. Further conclusions cannot be drawn from the low quality of the present XRD data.

5.3.3 SEM

SEM images of the as-sintered and reduced Gd_6WO_{12} samples are shown in figure 5.14. Clearly, the microstructure is altered and grains show signs of cracking or erosion which is consistent with the low crystallinity observed by XRD. Furthermore, the surface is covered by evenly distributed spherical particles with a diameter of approximately

[4]The Si-substrate gives no amorphous background which is inevitable with a glass substrate and is cut in a direction to give no reflections in XRD.

[5]The $RE_{3.43}W_{0.57}O_{6.85}\square_{1.15}$ representation of RE_6WO_{12} may serve for a better comparison with the oxynitride stoichiometry (section 3.1.2).

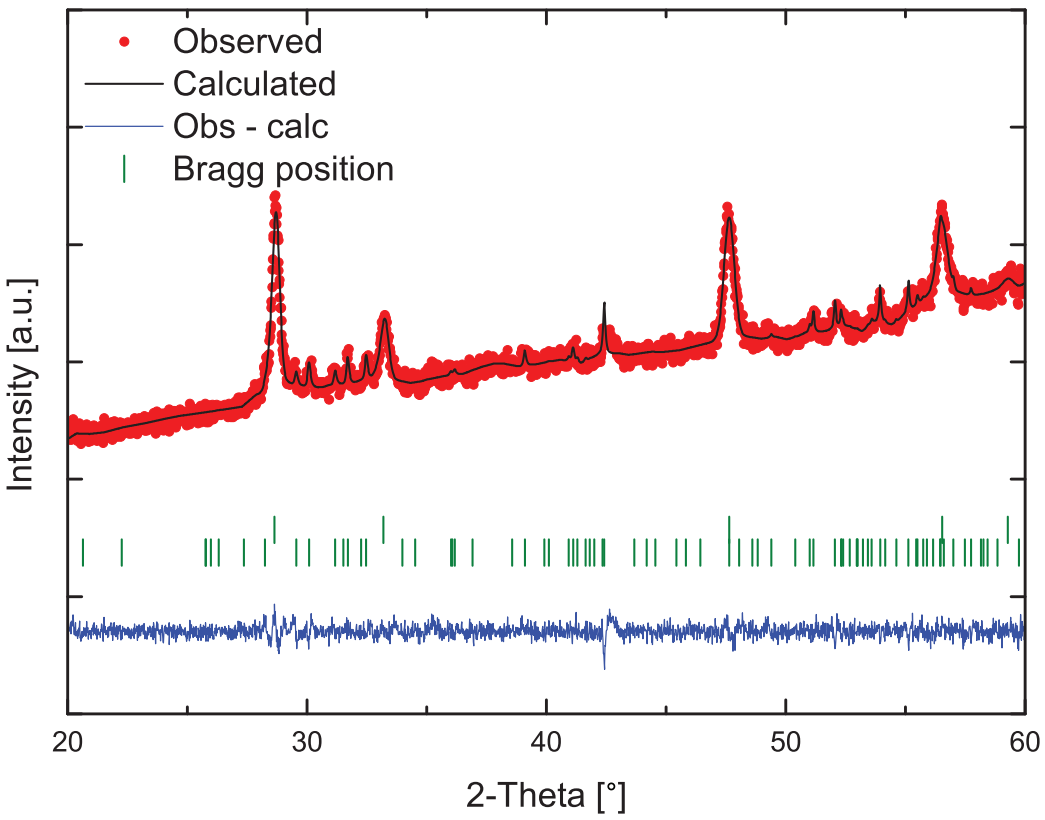

Figure 5.13: *XRD diffractogram of the reduced Gd_6WO_{12} sample fitted to the $Fm\bar{3}m$ space group (top Bragg position) and Gd_2O_3 (bottom Bragg position). Gd_2O_3 (C 2/m) segregated during synthesis (section 4.1).*

100 nm. These are bright in the back-scattered-electron image, which is indicative of a phase of heavier element(s). It is possible that these particles consist of metallic tungsten, which is thermodynamically more stable than the tungsten oxides under the conditions that the Gd_6WO_{12} sample was reduced under (1000 °C, $p_{O_2} \sim 10^{-24}$) [16]. Unfortunately, the nanoscopic size of the particles prevented compositional analysis by EDS. Moreover, considering the noise present in the diffractogram (figure 5.13) and the relatively low concentration of particles, they are not expected to appear in the diffractogram.

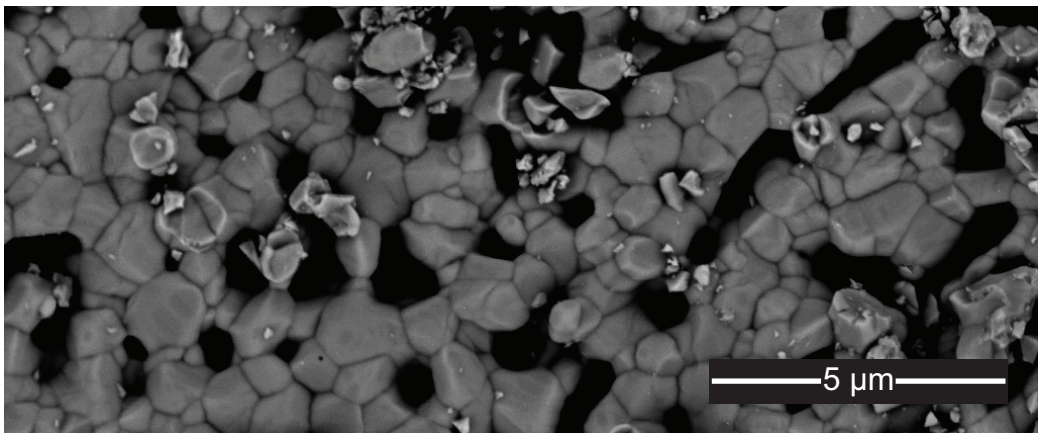

(a)

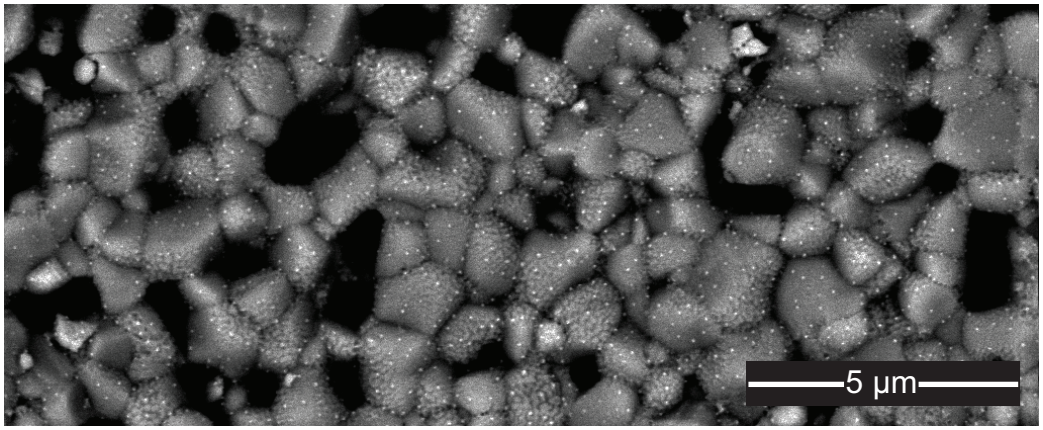

(b)

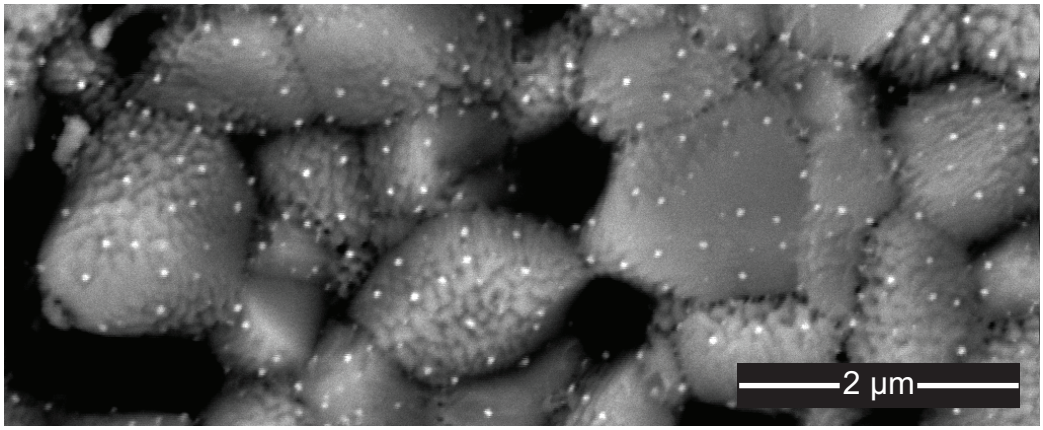

(c)

Figure 5.14: *SEM surface micrographs of Gd_6WO_{12} as-sintered (a) and after reduction (b & c) obtained with the SSD detector.*

5.4 Titanium dioxide — TiO_2

5.4.1 Conductivity

The conductivity of rutile TiO_2 was measured in NH_3, H_2 and N_2/H_2 mixtures at 700 °C. Figure 5.15 shows the conductivity during equilibration in ammonia and H_2 atmospheres. It can be seen that the initial reduction is both faster and more extensive in H_2, which is expected due to the lower p_{O_2} in H_2 compared to NH_3. Furthermore, it is evident that there is another process taking place in ammonia, resulting in a conductivity one order of magnitude higher than in H_2 after approximately 20 h. Even after more than 50 h the sample is not fully equilibrated in either NH_3 or H_2. During long term experiments, the behaviour of the sample was identical in H_2 and a N_2/H_2 mixture.

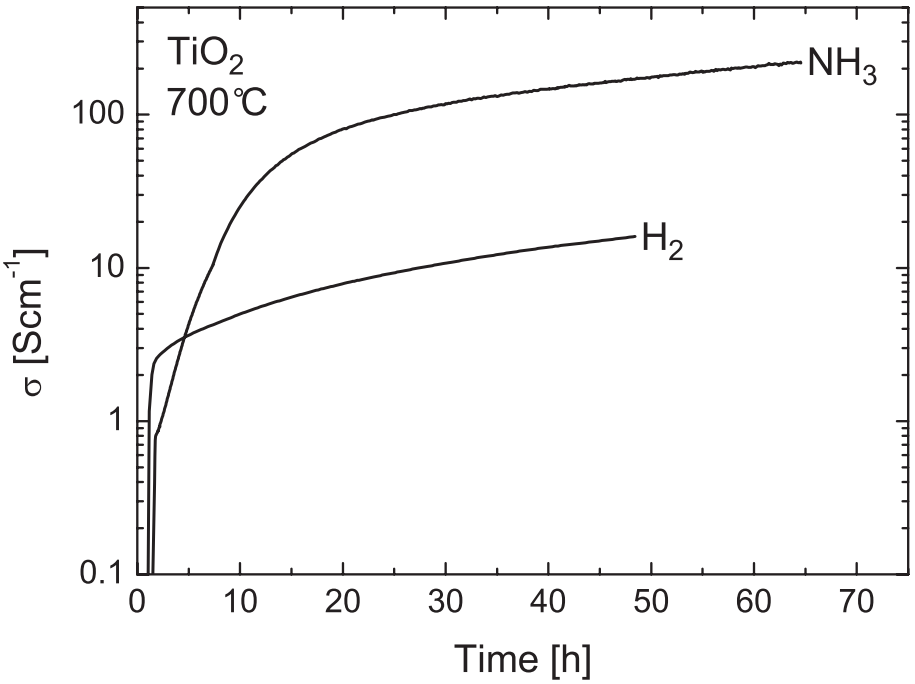

Figure 5.15: *Conductivity of a rutile TiO_2 sample in NH_3 and H_2 at 700 °C.*

Figure 5.16 shows temperature ramps in NH_3, H_2 and in Ar after the NH_3 treatment. The low temperature dependency of the conductivity for the NH_3 treated sample is consistent with non-activated transport (section 2.2). The argon ramp shows that the high conductivity achieved after NH_3 treatment is retained in this atmosphere, but starts to deviate at 250 °C. At 700 °C, the conductivity is fairly stable, and is reduced by only $2\,S\,cm^{-1}$ after 22 h, which may indicate a slow oxidation process.

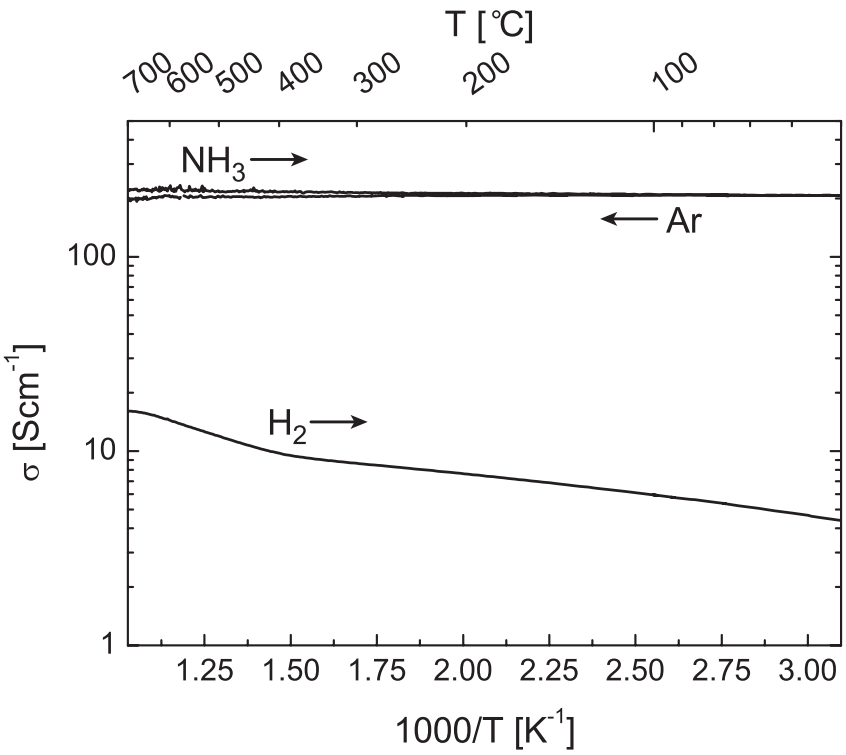

Figure 5.16: *Temperature ramps of rutile TiO_2 at 54 °C/h for H_2, NH_3 and up in Ar after the NH_3 ramp. The arrows indicate the direction of the ramp.*

5.4.2 XRD

Figure 5.17 shows an X-ray diffractogram of a rutile sample after ammonia treatment for 50 h at 700 °C and subsequent quenching to room temperature in the same atmosphere. New peaks emerged in between the reference patterns of TiO and TiN which implies formation of a titanium

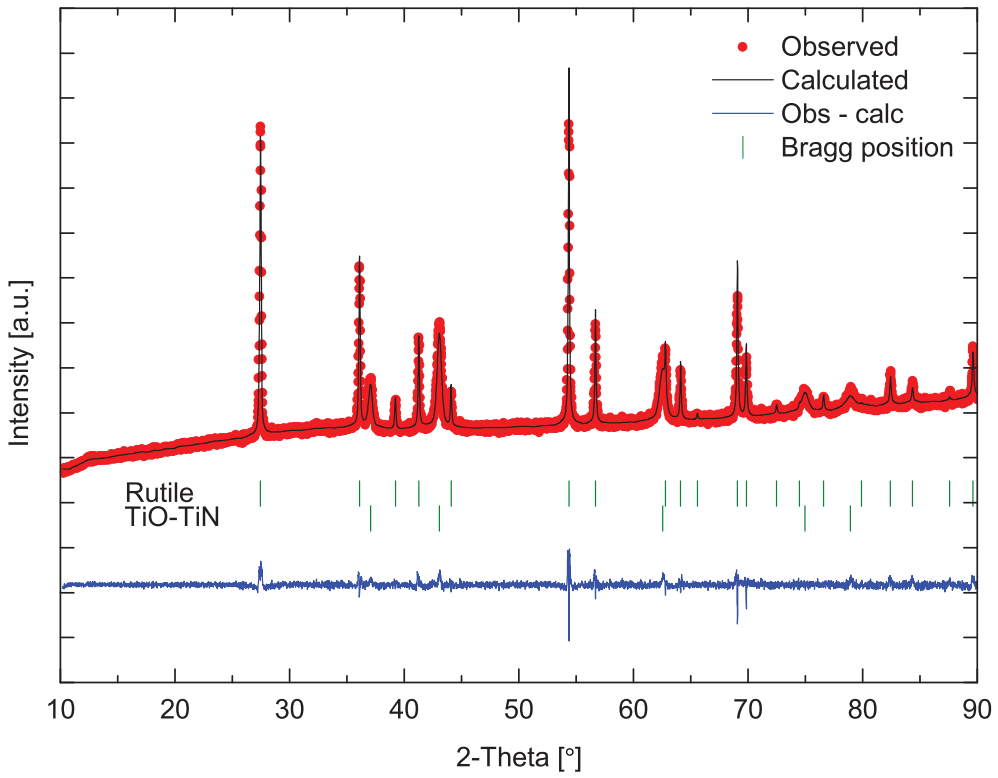

Figure 5.17: *X-ray diffractogram showing rutile TiO_2 and titanium oxynitride peaks.*

oxynitride phase. The lattice parameter of the new phase is shown in comparison with those of TiO and TiN in table 5.2.

The stoichiometry of the oxynitride phase was determined by Vegard's law by assuming a TiO_xN_{1-x} stoichiometry

$$a_{TiO_xN_{1-x}} = x\, a_{TiO} + (1-x)\, a_{TiN} \tag{5.1}$$

where a_{phase} denotes the lattice parameter of the respective phase.

Although it was pointed out in the literature review that TiO_xN_y is a more correct formula for the TiO—TiN solid solution (section 3.3.3), a TiO_xN_{1-x} stoichiometry is in this case considered a good approximation. First of all, the large non-stoichiometry reported by Martin *et al.* [68] can quite possibly be attributed to the kinetically controlled synthesis route (section 3.5.2). In addition, since TiO did not form in the sample quenched in hydrogen, oxygen deficiency in the oxynitride is not plausible.

Table 5.2: *Lattice parameters of the rutile TiO_2 and oxynitride phase compared with reference data for rutile TiO_2, TiO and TiN. Refinement parameters: Zero-point = 0.0362 °, $\chi^2 = 3.71$. t = tetragonal, c = cubic.*

Phase	**Refined data [Å]**	**Referance data [Å]**	
t-TiO_2 (rutile)	4.59(1)	4.5933	PDF: 21-1276
	2.95(1)	2.9592	
c-TiO	—	4.18500	PDF: 77-2170
c-$TiO_{0.64}N_{0.36}$	4.20(1)	—	
c-TiN	—	4.24173	PDF: 38-1420

Reduction of TiO_2 with ammonia has been reported in a patent by Shibuta *et al.* [77] where TiO, and not an oxynitride phase, is reported as the product. The present work, however, indicates that transition into the cubic phase is facilitated by nitrogen incorporation. In this respect, DFT calculations on anatase TiO_2 by Valentin *et al.* [4] showed a drastic reduction in the formation energy of oxygen vacancies in the presence of nitrogen (section 3.4.2). Considering the similarities between the anatase and rutile form of TiO_2 and the observed phase transition in the present work, the theoretical prediction made by Valentin *et al.* [4] seems to apply to rutile TiO_2 as well.

Since both TiO and TiN are metallic [78, 79], the low temperature dependency on the conductivity that was observed for the ammonia treated sample (figure 5.16), can be attributed to the partial transition into $TiO_{0.64}N_{0.36}$. Martin *et al.* [68] measured the conductivity of TiO—TiN films and obtained similar conductivity data as in the present work (section 3.5.2). The non-metallic temperature dependency was attributed to effects of grain boundary scattering typically seen in polycrystalline metallic materials.

5.4.3 GPA–MS

GPA-MS confirmed the presence of nitrogen in the ammonia treated sample. Unexpectedly, hydrogen also gave a substantial contribution to the total pressure. A similar experiment carried out with the TiO_2 sample reduced in hydrogen, gave no increase in pressure, except due to some water during the initial heating. Thus, incorporation of hydrogen is attributed to the ammonia treatment.

Subsequently, XRD analysis of the ammonia treated sample showed suppression of the oxynitride peaks, but no shift in their position. This implies a reduction in the amount of oxynitride phase but no alteration of the oxynitride stoichiometry.

5.4.4 Color

During the reduction and nitridation experiments, the sample went through changes in color. These are shown in figure 5.18. The yellow color after the GPA-MS experiment is attributed to segregation of a thin surface layer of TiN, which is yellow. The formation of this phase can be explained by the higher temperature that the sample was exposed to in the GPA-MS experiment, 800 °C, compared to in the ammonia treatment, 700 °C.

(a) (b) (c)

Figure 5.18: *Color of rutile samples; a) white: as-sintered, b) dark blue: reduced in H_2 (700 °C, 117 h) and c) dark red: quenched in ammonia (left) and yellow: after the GPA-MS experiment (right). The unevenness of the sample surfaces stems from the die used during sample preparation.*

5.5 Zinc oxide — ZnO

Conductivity measurements on ZnO samples were carried out at 500–700 °C in H_2/Ar and ammonia. Under these conditions, the dissolution of hydrogen donors in ZnO is substantial and the conductivity is dominated by this process in ammonia (section 3.1.5).

An attempt was made to anneal out hydrogen defects at 500 °C after a NH_3 treatment at 700 °C. However, the conductivity was affected by the evaporation and reduction of ZnO, which prevented a direct comparison between the effects of hydrogen mixtures and ammonia. Thus, it was concluded that such experiments were not suitable to probe the effects of nitrogen in ZnO.

5.6 XPS

XPS was utilized to investigate whether nitrogen could be detected in the samples which in conductivity measurements were affected by ammonia treatment.

Table 5.3 shows the conditions under which the specimens were treated prior to XPS analysis. The surface of the second 8YSZ specimen was covered by a porous layer of platinum to investigate possible catalytic activity towards nitrogen incorporation from N_2 gas. The porous Pt-layer was removed with a scalpel blade prior to analysis.

Only in 3YSZ and ZnO was nitrogen detected in the pure oxide structure. Figure 5.19 shows the XPS spectra of the N 1s region for these compounds. One nitride peak was identified in the 3YSZ spectrum and the nitrogen content was quantified to 3.5 at %. In the case of ZnO, the spectrum was fitted with three components. The main component at 396.3 eV is attributed to the nitride peak [80], while the other two components are not unambiguously ascribed to specific chemical states of nitrogen. A binding energy of 399–400 eV has previously been assigned to nitrogen species which are chemically bound to hydrogen [62, 81]. Given that NH_3 was used as nitrogen source, it is probable that component 3 in figure 5.19(b) represents a N-H related defect. The nitrogen content in

Table 5.3: *Sample treatment prior to XPS analysis for the samples that did not show nitride formation. All samples were quenched in the atmosphere that is listed and the N_2/H_2 atmosphere was a 1:3 mixture.*

Specimen	**Atmosphere**	**Temperature**	**Time**	**Comment**
		°C	h	
8YSZ	$N_2 + H_2$	1200	12	surface
8YSZ	$N_2 + H_2$	1200	12	surface, Pt-paint
3YSZ	NH_3	1200	77	surface
Er_2O_3	NH_3	700	22	surface
Y_2O_3	NH_3	1200	4	cleaved
ZnO	NH_3	700	20	cleaved

the ZnO specimen was quantified to 2.9 and 5.2 at % based on the N 1s component and all tree components, respectively.

Some specimens were cleaved in vacuum inside the XPS and subsequently analyzed in the freshly exposed surface. This was done to compare surface and bulk, and specifically to address the possibility of nitrogen residing only in one of these parts.

Based on the results from 3YSZ and ZnO, the detection limit for nitrogen can be estimated to approximately 0.5–1 at %. This fits quite well with the low S/N ratio in the XPS spectrum recorded by Jorge *et al.* [51] for 3 at % N in CeO_2 (figure 3.4). Thus, a lower nitrogen concentration in the RE_2O_3 compounds may account for why nitrogen was not detected by XPS although conductivity measurements suggest the presence of nitrogen defects.

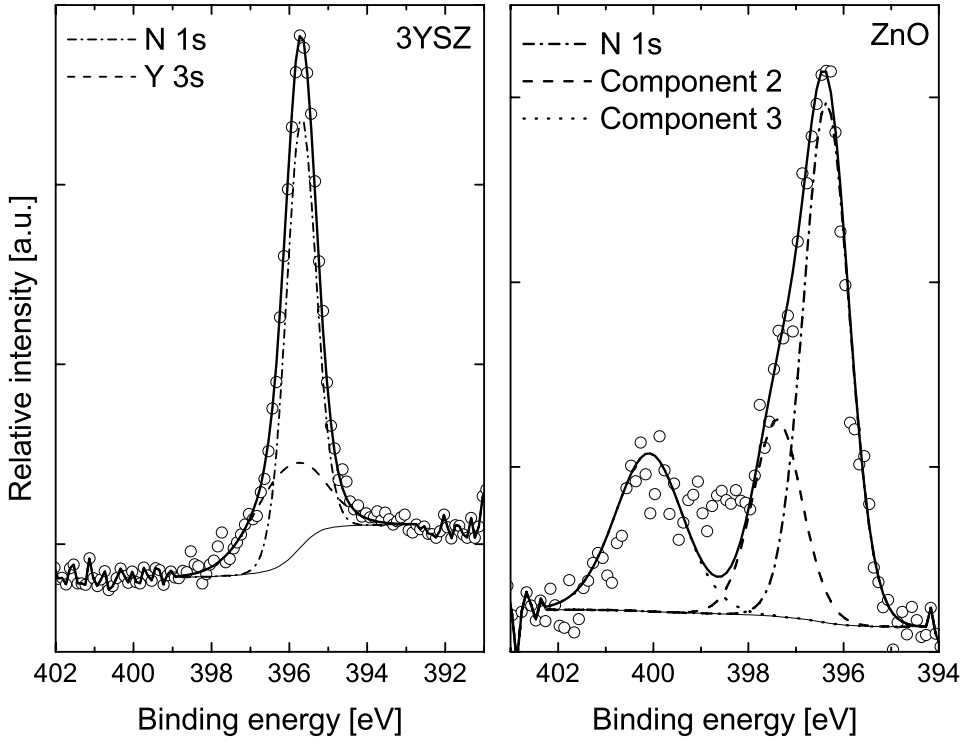

(a) (b)

Figure 5.19: *XPS spectra of the N 1s region. a) 3YSZ: The position of the Y 3s component was determined by applying the same chemical shift relative to tabulated values as was observed for the Y 3d peak. Furthermore, the peak area was determined by comparison with the Y 3d peak and their relative sensitivity factors. b) ZnO: N 1s and a proposed fitting for two additional components.*

Chapter 6

Discussion

Disregarding formation of nitrides or oxynitrides, the most prominent effect of ammonia was the increase in conductivity, not during ammonolysis, but after the ammonia containing environment was removed. In order to describe this behaviour, the following discussion is based on a model consisting of two parts: alteration of the defect structure due to acceptor doping; and dissolution and dissociation of N-H associate defects. The basic concepts are first treated for the RE_2O_3 compounds and then later applied to ZrO_2 and RE_6WO_{12}.

6.1 Part I: Defect structure

For the rare-earth sesquioxides, electronic conduction predominates at the high temperatures that the compounds were characterized at in the present work (section 3.1.1). The conductivity is then predominately *p*-type and *n*-type at high and low p_{O_2}, respectively, with a minimum in between which typically lies below the p_{O_2} obtained in argon (*i.e.* $p_{O_2} \sim 10^{-5}$ bar). Thus, the conductivity in hydrogen and ammonia is ascribed to electrons while that in argon and air is attributed to holes.

Due to the lower mobility of ionic charge carriers, it is reasonable to assume that the high conductivity that was obtained after ammonia treatment is electronic. Furthermore, since the high conductivity occurred in argon atmosphere, which normally gives *p*-type conductivity, holes are

proposed as the main charge carrier. The increased conductivity must then be a result of dissolution of nitrogen acceptors as a majority defect which is compensated by holes in the $p_{O_2} \sim 10^{-5}$ bar region.

However, this explanation alone fails to describe a crucial aspect: the conductivity was nearly unaffected in ammonia atmosphere. As mentioned in chapter 2, acceptor doping also suppresses negatively charged defects, which in this case would mean that a continuous lowering of the *n*-type conductivity should coincide with the dissolution of acceptors. Subsequently, *p*-type conduction should predominate also under reducing conditions if the dopant becomes a majority defect. One possibility may be that nitrogen acceptors are compensated by oxygen vacancies, which do not contribute significantly to conductivity, under reducing conditions and holes under more oxidizing conditions. This situation will be addressed at a later stage in conjunction with the discussion of the results for zirconia. In the following section, substitutional N-H defects are proposed to account for the shortcomings explained here.

6.2 Part II: N-H complexes

In hydrogen containing atmospheres, such as in ammonia, nitrogen can be incorporated as substitutional $NH_O^\times$ complexes

$$NH_3(g) + O_O^\times = NH_O^\times + H_2O(g) \tag{6.1}$$

Since this defect has no effective charge, it does not affect electroneutrality. Thus, this reaction is in compliance with the conductivity being the same in ammonia and a H_2/N_2 or H_2/Ar mixture of the same p_{O_2} (figure 5.1). However, when the hydrogen containing atmosphere is replaced by an inert gas, dissociation of the N-H complex can lead to activation of the dopant, $NH_O^\times \rightarrow N_O'$, through the formation of holes

$$NH_O^\times = N_O' + h^\bullet + \tfrac{1}{2}H_2(g) \tag{6.2}$$

The simplified electroneutrality condition is then written $p = [N_O']$, which is the same situation that was used to describe the high conductivity in the

previous section. However, the process that leads to the conductivity peak is now attributed to out-diffusion of hydrogen in addition to the increased p_{O_2}.

When the nitriding atmosphere is removed, the nitride substituents are gradually oxidized by impurities of O_2 in the inert gas while holes are consumed

$$\tfrac{1}{2}O_2(g) + N'_O + h^\bullet = O^\times_O + \tfrac{1}{2}N_2(g) \tag{6.3}$$

With respect to the concentration of charge carriers, the latter processes (reaction 6.2 and 6.3) counteract each other. Thus, there is a peak in conductivity followed by a decrease where reaction 6.3 is dominating (figure 5.1). Finally, the sample is equilibrated in the inert gas.

Furthermore, the behaviour upon introducing hydrogen at the conductivity peak (figure 5.2(b)) is proposed to represent a shift to the left in the equilibrium of reaction 6.2, which then seems to be readily reversible under these conditions. On the other hand, for a longer duration in hydrogen after the peak, conductivity did not rise again when returning to an inert gas (not shown). Considering that the atmosphere is not nitriding, the equilibrium in reaction 6.1 is shifted away from the products. Thus, out-diffusion of nitrogen is expected and this process is then assumed to also run in parallel with that in reaction 6.3.

In summary, the overall behaviour according to this model reflects a kinetically determined time frame where dissociation of the N-H complex and out-diffusion of hydrogen is faster than that of nitrogen.

6.2.1 Zirconia & rare-earth tungstates

It is well known that cubic stabilized ZrO_2 shows high oxide ion conductivity with negligible electronic contributions even at high temperatures (section 3.1.3). Thus, in the case of 3YSZ, the conductivity peak is attributed to the formation of oxygen vacancies

$$2NH^\times_O + O^\times_O = 2N'_O + v^{\bullet\bullet}_O + H_2O(g) \tag{6.4}$$

However, upon introducing hydrogen at the conductivity peak, there is no possibility for this reaction to be reversed due to lack of oxygen in

the atmosphere. This agrees well with the experimental results for 3YSZ, where only a slight decrease in conductivity was observed in hydrogen (figure 5.8(b)).

Thus, as the conductivity peak was observed to be completely suppressed in H_2 in the case of RE_2O_3 (figure 5.2(b)), formation of oxygen vacancies rather than holes is considered incompatible with the results that were obtained for RE_2O_3.

The inferior conductivity peak in 3YSZ compared to ZrO_2 can be explained by a lower solubility of additional negative defects in the presence of Y-acceptors as observed by Gutzov and Lerch [82].

In the case of pure ZrO_2, the conductivity was continuously increasing in ammonia which is attributed to formation of an oxynitride phase, $Zr_7O_8N_4$ (figure 5.8(a)). This indicates a higher conductivity of $Zr_7O_8N_4$ compared to the pure oxide, although it is reported to be lower than similarly Y-doped ZrO_2 (section 3.5.1). The conductivity peak can then be attributed to formation of oxygen vacancies in the oxide phase in the same manner as for 3YSZ. The lower conductivity peak at higher temperatures may be explained by an accelerated formation of the oxynitride phase, and thus a lower concentration of nitrogen acceptors in the pure oxide.

A similar argumentation may be used to explain the lower conductivity peak for longer ammonolysis times in the case of RE_6WO_{12} as seen for RE = Gd in figure 5.10. However, since RE_6WO_{12} are good electronic conductors (section 3.1.2), holes are expected to be the dominating charge carrier at the conductivity peak.

6.2.2 Stability: $NH_O^\times$ vs. $N_O^/$

As mentioned in the literature review, N-H complexes have previously been identified in ZnO and TiO_2. Furthermore, in the case of ZnO, dissociation of the N-H complexes and out-diffusion of hydrogen has been achieved by annealing at appropriate temperatures to successfully produce a *p*-type material (section 3.4.3). This is the same process that is suggested to describe the results obtained in the present work.

In ZnO, which dissolves hydrogen directly from H_2 gas, association

between N'_O and $H_i^\bullet$ was shown to be energetically preferable by DFT studies (section 3.4.3). The present work gives evidence that N-H complexes are favorable also in oxides which do not readily dissolve hydrogen from H_2 gas. Furthermore, measurements indicate that hydrogen in N-H complexes can exist in equilibrium with the surrounding atmosphere and that the concentration of N-H complexes relative to nitride substituents varies with p_{H_2}. However, one may speculate whether this is because nitrogen is incorporated only in the outermost surface of the material where the nitrogen defects are accessible from the surrounding atmosphere. Although the RE_2O_3 compounds primarily dissolve protons from water [83], dissolution of hydrogen from H_2 gas occurs as well, only to a lesser extent. Thus, N-H association in these compounds can be explained by a similar argumentation as with ZnO.

The reason for $NH_O^\times$ being the preferred nitrogen defect, at least under reducing conditions, is quite possibly related to the formation energy of the compensating defect that must form in conjunction with N'_O, *e.g.* holes or oxygen vacancies.

6.3 Comparison between the compounds

6.3.1 Nitrogen incorporation

This section will elaborate on some aspects of thermal ammonolysis of oxides in light of the results that were obtained in this work.

It is reasonable to assume that the temperature at which an oxide reacts with ammonia is related to the formation enthalpy of the oxide and, if it exists, that of the corresponding nitride. This description can qualitatively account for the different temperatures at which reaction with ammonia was observed: the most stable oxide, Y_2O_3, required 1200 °C to react with ammonia, while ammonolysis was observed already at 700 °C for the least stable oxides, ZnO and TiO_2[1]. However, even though the enthalpy of formation of rutile TiO_2 is almost three times as large as that

[1] Based on the standard enthalpies of formation according to HSC [16].

of ZnO, considerably more nitrogen was incorporated into the former oxide. Reaction with ammonia was observed at 700 °C also for RE_6WO_{12}. This may be attributed to the fact that relatively stable oxynitrides and nitrides exist in the Ti—O—N and RE—W—O—N systems, which is not the case for the Zn—O—N system [16]. Moreover, Jorge *et al.* [51] found a maximum nitrogen uptake of 3 at % in CeO_2 at 700 °C (section 3.4.1). By comparison with rutile TiO_2 and TiN, CeO_2 is more stable than TiO_2 and CeN is less stable than TiN, which may explain why Jorge *et al.* [51] did not obtain any nitrides or oxynitrides of cerium.

Elder *et al.* [1] claim that nitridation of oxides is driven by the formation of water, as facilitated by formation of oxygen vacancies, and to a lesser extent by the free energies of formation of the binary oxides and nitrides. Furthermore, according to reaction 2.5, which can be asserted to be a defect chemical analogue to nitride/oxynitride formation, stable oxygen vacancies will increase nitrogen incorporation. In this respect, rutile TiO_2 and ZnO represent opposites, where $v_O^{\bullet\bullet}$ are particularly preferable in rutile TiO_2 and unstable in ZnO (section 3.1), which may explain their different reactivities towards ammonia. Furthermore, oxygen vacancies are preferable also in ZrO_2, which may explain the oxynitride formation by reaction with ammonia. However, CeO_2 showed only intermediate level of nitrogen incorporation even though it can accommodate considerable amounts of oxygen vacancies [84].

Incorporation of substitutional N-H complexes can be viewed as formation of an oxygen vacancy followed by a nitridation step

$$O_O^{\times} = v_O^{\bullet\bullet} + 2e' + \tfrac{1}{2}O_2(g) \quad (6.5)$$

$$NH_3(g) + v_O^{\bullet\bullet} + 2e' = NH_O^{\times} + H_2(g) \quad (6.6)$$

$$\overline{NH_3(g) + O_O^{\times} = NH_O^{\times} + H_2O(g)}$$

where the total reaction is the same as reaction 6.1. This view can be considered more appropriate to evaluate the compounds which showed indications of N-H complexes and which did not undergo phase transformation upon ammonolysis.

From these partial reactions, it can be seen that formation of oxygen vacancies is a prerequisite for nitrogen incorporation, and that an increased oxygen vacancy concentration will, according to Le Chatelier's principle, drive the nitridation forward. However, from reaction 6.6, it is clear that the level of nitrogen incorporation depends on the stability of the N-H complex relative to the oxygen vacancy. In this respect, since nitrogen is "oxidizing", it may be anticipated that reaction 6.6 is quite favorable for many oxides.

The fact that the *n*-type conductivity of the RE_2O_3 compounds, given by reaction 6.5 (section 3.1.1), was constant during ammonolysis (section 5.1), points towards oxygen vacancies not being depleted during nitrogen substitution. Thus, it seems that N-H substituents do not suppress the concentration of oxygen vacancies, which is reasonable also by considering the electroneutrality condition due to the effectively neutral charge of $NH_O^{\times}$. The conductivity also remained constant during ammonolysis of 3YSZ (section 5.2). However, the charge carrier concentration is in this case determined by Y-acceptors rather than reaction 6.5. Thus, reaction 6.6 cannot be evaluated based on the conductivity data of 3YSZ.

6.3.2 Conductivity of RE_2O_3:N and YSZ:N

According to the model based on N-H complexes, the conductivity peak as it is perceived in experiments represents a transition between two defect situations: *n*-type conductivity in ammonia and subsequently *p*-type predominance determined by nitrogen acceptors in argon. In order to evaluate the effect of nitrogen incorporation, figure 6.1 shows the conductivity in argon before and after ammonolysis of the RE_2O_3 compounds.

However, for these measurements there exists no point of reference to relate the conductivity obtained in argon after ammonolysis to the concentration of nitrogen acceptors. Furthermore, the values in figure 6.1 may be governed by different background levels of donor and acceptor-type impurities. Thus, difficulty arises when comparison between the

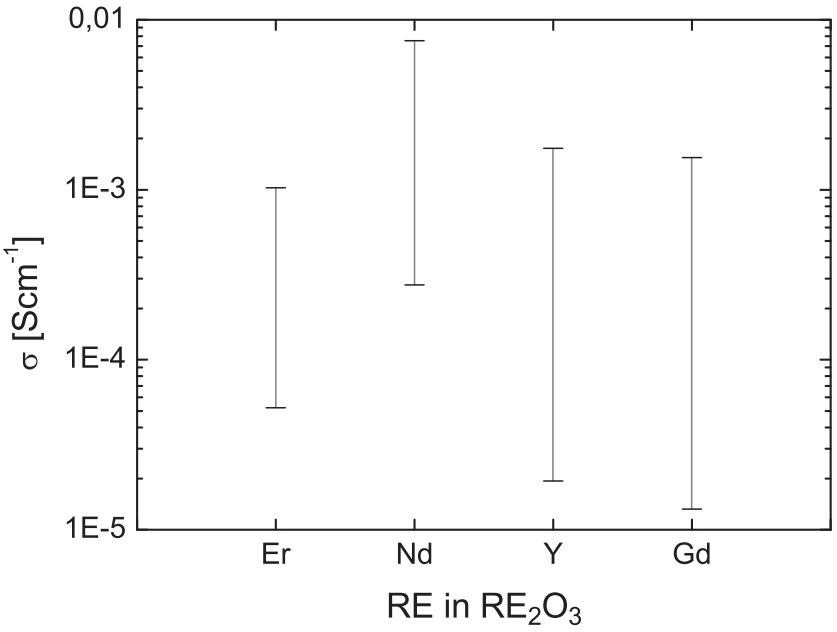

Figure 6.1: *Difference in conductivity before and after ammonia treatment in argon for RE_2O_3 at 1200 °C.*

compounds is attempted.

In the case of Y_2O_3, the concentration of nitrogen can be quantified from the GPA-MS results (section 5.1.1). Based on the volume and total pressure in the sample chamber, mass of the specimen and by assuming a 1:1 ratio between nitrogen and hydrogen[2], a $NH_O^\times$ concentration of 0.13 at % is obtained. In figure 6.2, this value and corresponding conductivity data is compared with the relative increase in conductivity upon CaO-doping as reported by Katayama *et al.* [22] (section 3.1.1). By considering the relative conductivities, only the concentration of charge carriers is varied with doping and comparison between different temperatures and atmospheres can be considered acceptable.

As both the nitrogen quantification from GPA-MS and the basis for this comparison is accompanied with uncertainties, the data is asserted to

[2]Hydrogen intensities were found to be associated with considerable uncertainties in GPA-MS analysis (section 4.2.4). A 1:1 ratio between nitrogen and hydrogen is based on the defect model with $NH_O^\times$, and can be assumed within the deviations that were observed with the calibration gas.

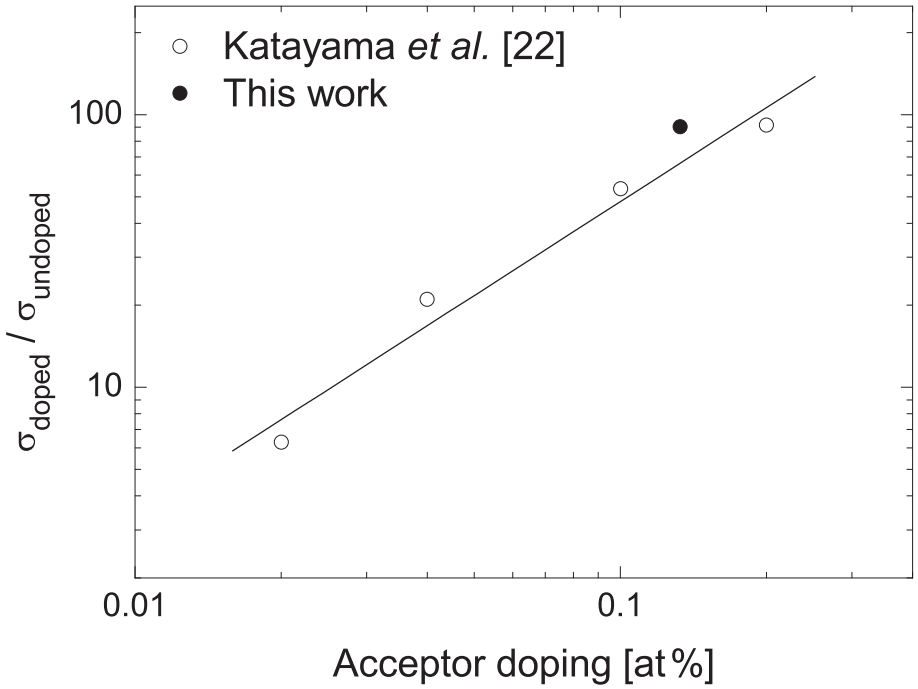

Figure 6.2: *Relative difference in conductivity of nominally undoped and acceptor doped Y_2O_3 as a function of acceptor doping concentration. Data from Katayama et al. [22] represents conductivity in dry air at 977 °C with Ca-doping and a linear fit based on $\sigma_i = z_i e c_i u_i$ (section 2.2). This work represents the nitrogen concentration as determined from GPA-MS and values for Y_2O_3 from figure 6.1 i.e. in Ar at 1200 °C.*

be in semi-quantitative agreement. Furthermore, by comparison with the estimated detection limit for XPS, the nitrogen concentration obtained here also explains why nitrogen was not detected in the RE_2O_3 compounds with XPS (section 5.6).

In the case of the 3YSZ sample, the conductivity peak at 1000 °C (figure 5.8(b)) represents a 1.5 times increase in conductivity, which by assuming pure oxide ion conductivity, corresponds to the same increase in acceptors relative to the 1.95 at % of yttrium (section 3.5.1). Accordingly, a nitrogen concentration of 2.9 at % can be predicted from the conductivity data, which is slightly lower than the 3.5 at % from the XPS quantification of 3YSZ treated at 1200 °C (section 5.6). Since the solubility

of nitrogen defects is expected to increase with temperature (section 2.1), the conductivity data is considered to be in accordance with the nitrogen quantification of 3YSZ.

6.4 Future work and additional thoughts

In light of results and discussion presented in this work, further investigation to unambiguously uncover the defect chemical processes taking place during and after equilibration of oxides in ammonia atmosphere, is called for. In this respect, gas chromatography or MS analysis of the outlet gas from the measurement cell can be used to accurately determine the partial pressure of ammonia in the system. Furthermore, with this setup, experiments may be designed to analyze release of hydrogen upon dissociation of the proposed $NH_O^\times$ complexes.

Out of the compounds characterized in this work, the rare-earth sesquioxides were found to be the most appropriate for investigation of nitrogen *defects*. Because of the high stability of these oxides, they contain low concentrations of intrinsic defects which enables nitrogen to function as a predominating defect. Further measurements on these compounds are necessary to determine the temperature dependency of both nitrogen incorporation and dissociation of N-H complexes.

In order to extract nitrogen acceptor concentrations from conductivity data, a small, but dominating, cation acceptor concentration may serve as a reference level. With the simplified electroneutrality condition

$$[\mathrm{Acc}'] + [\mathrm{N}'_\mathrm{O}] = \mathrm{p} \tag{6.7}$$

the concentration of nitrogen can be related to the concentration of cation acceptors, which is known, by observing changes in conductivity due to variation in the concentration of holes. Furthermore, through nitrogen quantification with GPA-MS or SIMS, the validity of the model can be evaluated. Regarding N-H complexes, hydrogen can also be quantified by SIMS and development of reliable sample preparation routines for IR analysis may also play an important role in characterizing these defects. Moreover, it may be noted that a defect complex in which the hydrogen

passivator resides on an adjacent oxygen atom, $\left(N'_O\text{-}OH^{\bullet}_O\right)^{\times}$, is equally effective in describing the observed results as the $NH^{\times}_O$ complex. In this respect, IR analysis is of interest to determine the possibility of a $\left(N'_O\text{-}OH^{\bullet}_O\right)^{\times}$ complex, especially in compounds where protons in the form of $OH^{\bullet}_O$ are particularly stable.

Incorporation of other types of nitrogen defects may require a nitrogen source different from ammonia. A nitriding gas which also is oxidizing, *e.g.* NO_2 or N_2O, is not expected to give anion substitutional nitrogen defects. However, as mentioned in section 2.1.2, nitrogen interstitials may be energetically preferred over oxygen interstitials. Dissolution of N_i''' will give a different pressure dependency on the concentration of charge carriers than O_i'', which means that they can be identified by conductivity measurements. In this case, thermodynamic parameters for dissolution of nitrogen defects can be extracted.

From a theoretical point of view, *ab initio* calculations can be a powerful tool to determine the stability of various nitrogen related defects. Particularly, these methods enable investigation of individual types of defects and their properties irrespective of other defects present in the system.

6.4.1 Nitrogen and proton conduction

Nitrogen doped proton conducting oxides are of interest to investigate effects of anion doping on dissolution and transport of protons. Such a study may, however, be restricted to low temperatures where substitutional nitrogen can be stable under wet conditions.

Since proton transport typically proceeds through the anion sub-lattice [85] *i.e.* Grotthus mechanism, it is likely that anion doping has a greater impact on mobility than cation doping. By electrostatic considerations, it is reasonable that nitrogen acts as a proton trap. However, acknowledging the importance of oxygen sub-lattice dynamics for proton mobility [85], the effect of nitrogen is likely to be more complicated. Furthermore, formation of $NH^{\times}_O$ can be viewed as dissolution of protons, but these protons may not contribute to proton conductivity if mobility is reduced.

Thus, the effect of using ammonia as energy carrier in a proton conducting solid oxide fuel cell remains uncertain and will quite probably differ depending on the electrolyte material.

Existence of N-H type defects in oxides, brings attention to the possibility of equivalent protonic defects in nitrides. By analogy with the hydration reaction in an oxide

$$H_2O(g) + O_O^{\times} + v_O^{\bullet\bullet} = 2OH_O^{\bullet} \tag{6.8}$$

a similar reaction for dissolution of protons in nitrides

$$NH_3(g) + 2N_N^{\times} + v_N^{\bullet\bullet\bullet} = 3NH_N^{\bullet} \tag{6.9}$$

may in some compounds be equally important as the hydration reaction is in many oxides. Furthermore, investigation of protons in nitrides may contribute to understanding the behaviour of protonic species in solid state materials with the anion as a new variable. In this respect, whether the Grotthus mechanism also applies to nitrides is an intriguing question.

Chapter 7

Conclusion

Nitrogen incorporation was found to be significant in terms of influencing the electrical properties and/or structure for all the investigated oxides when equilibrated in ammonia atmosphere at sufficiently high temperatures.

A defect model based on $NH_O^\times$ complexes, in which the hydrogen passivator exists in equilibrium with atmosphere, can effectively account for the observed results from conductivity measurements on 3YSZ and the RE_2O_3 compounds. In the case of Y_2O_3 and 3YSZ, the conductivity data, as interpreted according to the proposed defect model, was found to be in semi-quantitative agreement with nitrogen quantification by GPA-MS and XPS, respectively. Furthermore, conductivity measurements of the RE_6WO_{12} compounds could be explained with the same defect model except at higher temperatures where a phase transformation, possibly into an oxynitride, was observed. Thus, the present work indicate N-H complexes to be an important nitrogen related defect in oxides beyond those reported in literature *i.e.* ZnO and TiO_2. However, further investigation is necessary to unambiguously determine the nature of the processes underlying the results obtained from conductivity measurements.

Electrical characterization in ammonia atmosphere was found to be unsuitable to investigate nitrogen defects in ZnO due to the predominance of donor type defects under reducing conditions *i.e.* $H_i^\bullet$. Furthermore,

results from thermal ammonolysis of rutile TiO_2 indicate that reduction to the cubic structure of TiO is facilitated by nitrogen incorporation through the formation of a TiO—TiN solid solution.

The present work has generated questions which are of interest for both academic and application based research.

Bibliography

[1] S.H. Elder, F.J. DiSalvo, L. Topor, and A. Navrotsky. Thermodynamics of ternary nitride formation by ammonolysis: application to $LiMoN_2$, Na_3WN_3, and Na_3WO_3N. *Chemistry of materials*, 5(10):1545–1553, 1993.

[2] R.D. Shannon. Revised effective ionic radii and systematic studies of interatomic distances in halides and chalcogenides. *Crystal Physics, Diffraction, Theoretical and General Crystallography*, 32(5):7394, 1976.

[3] Ü. Özgür, Y.I. Alivov, C. Liu, A. Teke, M.A. Reshchikov, S. Doğan, V. Avrutin, S.J. Cho, and H. Morkoc. A comprehensive review of ZnO materials and devices. *Journal of Applied Physics*, 98:041301–63, 2005.

[4] C. Di Valentin, E. Finazzi, G. Pacchioni, A. Selloni, S. Livraghi, M.C. Paganini, and E. Giamello. N-doped TiO_2: Theory and experiment. *Chemical Physics*, 339(1-3):44–56, 2007.

[5] K. Hashimoto, H. Irie, and A. Fujishima. TiO_2 Photocatalysis: A Historical Overview and Future Prospects. *Japanese Journal of Applied Physics part 1*, 44(12):8269, 2005.

[6] W. Choi, A. Termin, and M.R. Hoffmann. The Role of Metal Ion Dopants in Quantum-Sized TiO_2: Correlation between Photoreactivity and Charge Carrier Recombination Dynamics. *Journal of Physical Chemistry*, 98(51):13669–13679, 1994.

[7] P. Kofstad and T. Norby. Defects and transport in crystalline solids. Compendium for the advanced level course KJM 5120: Defect chemistry and Reactions in Solids, September 2007.

[8] B.G. Streetman and S. Banerjee. *Solid State Electronic Devices*. Prentice Hall, 2006.

[9] J. Maier. *Physical Chemistry of Ionic Materials: Ions and Electrons in Solids*, chapter 5.2, page 120. Wiley, 2004.

[10] F.A. Kroger and H.J. Vink. Relations Between the Concentrations of Imperfections in Crystalline Solids in Solid State Physics. *Academic Press, New York*, pages 307–435, 1956.

[11] I. Tanaka, K. Tatsumi, M. Nakano, H. Adachi, and F. Oba. First-Principles Calculations of Anion Vacancies in Oxides and Nitrides. *Journal of the American Ceramic Society*, 85(1):68–74, 2002.

[12] C.G. Van de Walle and J. Neugebauer. Universal alignment of hydrogen levels in semiconductors, insulators and solutions. *Nature*, 423(6940):626–628, 2003.

[13] J. Maier. *Physical Chemistry of Ionic Materials: Ions and Electrons in Solids*, chapter 6.2, page 293. Wiley, 2004.

[14] L. J. van der Pauw. A method of measuring the resistivity and hall coefficient of lamellae of arbitrary shape. *Phillips Technical Review*, 20(8):220–224, 1958.

[15] L. J. van der Pauw. A method of measuring specific resistivity and hall effects of discs of arbitrary shape. *Philips Research Report*, 13(1):1–9, February 1958.

[16] A. Roine. Hsc chemistry 4.1: Chemical reaction and equilibrium software with extensive thermochemical database, 2000. Outukumpu Reasearch Oy, Pori, Finland.

[17] M. Foex and J.P. Traverse. Investigations about crystalline transformation in rare earths sesquioxides at high temperatures. *Rev. Int. Hautes Temp. Refract*, 3(4):429–453, 1966.

[18] N.M. Tallan and R.W. Vest. Electrical Properties and Defect Structure of Y_2O_3. *Journal of the American Ceramic Society*, 49(8):401–404, 1966.

[19] M.F. Berard, C.D. Wirkus, and D.R. Wilder. Diffusion of Oxygen in Selected Monocrystalline Rare Earth Oxides. *Journal of the American Ceramic Society*, 51(11):643–647, 1968.

[20] H. Hartmanovà, E.Morhàčovà, I. Travěnec, A.A. Urusovskaya, and G.G. Knab. Defect structure and physical properties of Y_2O_3. *Solid State Ionics*, (36):137–142, 1989.

[21] R.J. Bratton. Defect Structure of Y_2O_3—ZrO_2 Solid Solutions. *Journal of the American Ceramic Society*, 52(4):213–213, 1969.

[22] K. Katayama, H. Osawa, and T. Akiba. Sintering and Electrical Properties of CaO-Doped Y_2O_3. *Journal of the European Ceramic Society*, 6:39–45, 1990.

[23] P. Kofstad. *Nonstoichiometry, diffusion, and electrical conductivity in binary metal oxides*. Wiley-Interscience New York, 1972.

[24] H.B. Lal and K. Gaur. Electrical conduction in non-metallic rare-earth solids. *Journal of Materials Science*, 23(3):919–923, 1988.

[25] G.J. McCarthy, R.D. Fischer, and G.G. Johnson. Crystal chemistry and compound formation in the systems rare-earth sesquioxide—WO_3. *Solid State Chemistry*, 1972.

[26] R. Haugsrud. Defects and transport properties in Ln_6WO_{12} (Ln = La, Nd, Gd, Er). *Solid State Ionics*, 178(7-10):555–560, 2007.

[27] M. Yoshimura. Phase stability of zirconia. *American Ceramic Society Bulletin*, 67(12):1950–1955, 1988.

[28] P. Kofstad. *Nonstoichiometry, diffusion, and electrical conductivity in binary metal oxides*. Wiley-Interscience New York, 1972.

[29] R.W. Vest, N.M. Tallan, and W.C. Tripp. Electrical properties and defect structure of zirconia. I – monoclinic phase. *Journal of American Ceramic Society*, 47:635–640, 1964.

[30] F. Millot, M.G. Blanchin, R. Tetot, J.F. Marucco, B. Poumellec, C. Picard, and B. Touzelin. High temperature nonstoichiometric rutile TiO_{2-x}. *Progress in solid state chemistry*, 17(4):263–293, 1987.

[31] T. Bak, M.K. Nowotny, L.R. Sheppard, and J. Nowotny. Mobility of Electronic Charge Carriers in Titanium Dioxide. *The Journal of Physical Chemistry C*, 112(33):12981–12987, 2008.

[32] G. Heiland, E. Mollwo, and F. Stockman. Electronic Processes in ZnO. *Solid State Phys*, 8:193, 1959.

[33] A.F. Kohan, G. Ceder, D. Morgan, and C.G. Van de Walle. First-principles study of native point defects in ZnO. *Physical Review B*, 61(22):15019–15027, 2000.

[34] A. Janotti and C.G. Van de Walle. Native point defects in ZnO. *Phys. Rev. B*, 76(16):165202–22, 2007.

[35] C.G. Van de Walle. Defect analysis and engineering in ZnO. *Physica B: Physics of Condensed Matter*, 308:899–903, 2001.

[36] C.G. Van de Walle. Hydrogen as a cause of doping in zinc oxide. *Physical Review Letters*, 85(5):1012–1015, 2000.

[37] Y.B. Cheng and D.P. Thompson. Role of anion vacancies in nitrogen-stabilized zirconia. *Journal of the American Ceramic Society*, 76(3):683–688, 1993.

[38] T.J. Chung, J.S. Lee, D.Y. Kim, and H. Song. Surface Nitridation of Yttria-Doped Tetragonal Zirconia Polycrystals (Y-TZP): Microstructural Evolution and Kinetics. *Journal of the American Ceramic Society*, 82(11):3193–3199, 1999.

[39] I. Valov. *Nitrogen doped zirconia (N-YSZ): preparation, characterization and electrode processes*. PhD thesis, Justus-Liebig-University Giessen, 2006.

[40] J. Gilles and R. Collongues. The structure and the properties of phases formed during the action of ammonia on zirconia. *Compt. rend*, 254, 1962.

[41] Y. B. Cheng and D. P. Thompson. The nitriding of zirconia. *British ceramic proceedings*, 49:149–162, 1992.

[42] M. Lerch. Nitridation of zirconia. *Journal of the American Ceramic Society*, 79(10):2641–2644, 1996.

[43] M. Lerch, J. Wrba, and J. Lerch. Vacancy Ordering in the ZrO_2 Rich Part of the Systems Ca–Zr–O–N, Mg–Zr–O–N, and Y–Zr–O–N. *Journal of Solid State Chemistry*, 125(2):153–158, 1996.

[44] J. Wrba and M. Lerch. Phase Relationships in the ZrO_2-rich part of the systems Y–Zr–N–O, Ca–Zr–N–O, and Mg–Zr–N–O up to temperatures of 1150 °C. *Journal of the European Ceramics Society*, 18(12):1787–1793, 1998.

[45] B.A. Shaw, Y.B. Cheng, and D.P. Thompson. Nitrogen Stabilization of Tetragonal Zirconias. *British ceramic proceedings*, pages 143–152, 1993.

[46] N. Diot, O. Larcher, R. Marchand, J.Y. Kempf, and P. Macaudière. Rare-earth and tungsten oxynitrides with a defect fluorite-type structure as new pigments. *Journal of Alloys and Compounds*, 323:45–48, 2001.

[47] F. Tessier and R. Marchand. Ternary and higher order rare-earth nitride materials: synthesis and characterization of ionic-covalent oxynitride powders. *Journal of Solid State Chemistry*, 171(1-2):143–151, 2003.

[48] B. Granier, R. Renard, and J.P. Coutures. Ternary Phase Diagram of Ti–O–N: Study of the TiO–TiN Cubic Solid Solution. *Revue Internationale des Hautes Temperatures et des Refractaires*, 17(3):235, 1980.

[49] X. Yang, C. Li, B. Yang, W. Wang, and Y. Qian. Optical properties of titanium oxynitride nanocrystals synthesized via a thermal liquid–

solid metathesis reaction. *Chemical Physics Letters*, 383(5-6):502–506, 2004.

[50] M. Drygás, C. Czosnek, R.T. Paine, and J.F. Janik. Two-Stage Aerosol Synthesis of Titanium Nitride TiN and Titanium Oxynitride TiO_xN_y Nanopowders of Spherical Particle Morphology. *Chem. Mater*, 18(13):3122–3129, 2006.

[51] A.B. Jorge, J. Fraxedas, A. Cantarero, A.J. Williams, J. Rodgers, J.P. Attfield, and A. Fuertes. Nitrogen Doping of Ceria. *Chem. Mater.*, 20:1682–1684, 2008.

[52] R. Asahi, T. Morikawa, T. Ohwaki, K. Aoki, and Y. Taga. Visible-Light Photocatalysis in Nitrogen-Doped Titanium Oxides, 2001.

[53] X. Gao, J.X. Shang, and Y. Zhang. First-Principles Study of Nonmetal-Doped Titanium Oxides. *Key Engineering Materials*, 336–338:2507–2509, 2007.

[54] J.Y. Lee, J. Park, and J.H. Cho. Electronic properties of N-and C-doped TiO. *Applied Physics Letters*, 87:011904, 2005.

[55] T. Lindgren, J.M. Mwabora, E. Avendano, J. Jonsson, A. Hoel, C.G. Granqvist, and S.E. Lindquist. Photoelectrochemical and Optical Properties of Nitrogen Doped Titanium Dioxide Films Prepared by Reactive DC Magnetron Sputtering. *Journal of Physical Chemistry B*, 107(24):5709–5716, 2003.

[56] M. Kitano, M. Matsuoka, M. Ueshima, and M. Anpo. Recent developments in titanium oxide-based photocatalysts. *Applied Catalysis A, General*, 325(1):1–14, 2007.

[57] M. Batzill, E.H. Morales, and U. Diebold. Influence of Nitrogen Doping on the Defect Formation and Surface Properties of TiO_2 Rutile and Anatase. *Physical Review Letters*, 96(2):26103, 2006.

[58] X. Li, B. Keyes, S. Asher, SB Zhang, S.H. Wei, T.J. Coutts, S. Limpijumnong, and C.G. Van de Walle. Hydrogen passivation effect in

nitrogen-doped ZnO thin films. *Applied Physics Letters*, 86:122107, 2005.

[59] S.J. Jokela and M.D. McCluskey. Unambiguous identification of nitrogen-hydrogen complexes in ZnO. *Physical Review B*, 76(19):193–201, 2007.

[60] J.G. Lu, S. Fujita, T. Kawaharamura, and H. Nishinaka. Roles of hydrogen and nitrogen in *p*-type doping of ZnO. *Chemical Physics Letters*, 441(1-3):68–71, 2007.

[61] J.G. Lu and S. Fujita. Hydrogen-assisted nitrogen-acceptor doping in ZnO. *Physica Status Solidi (a)*, 205(8), 2008.

[62] O. Diwald, T.L. Thompson, T. Zubkov, E.G. Goralski, S.D. Walck, and J.T.J. Yates. Photochemical Activity of Nitrogen-Doped Rutile TiO_2 (110) in Visible Light. *ChemInform*, 35(30), 2004.

[63] O. Diwald, T.L. Thompson, E.G. Goralski, S.D. Walck, and J.T. Yates Jr. The effect of nitrogen ion implantation on the photoactivity of TiO_2 rutile single crystals. *J. Phys. Chem. B*, 108(1):52–57, 2004.

[64] T. Yamamoto. Codoping for the fabrication of *p*-type ZnO. *Thin Solid Films*, 420:100–106, 2002.

[65] A. Kamata, H. Mitsuhashi, and H. Fujita. Origin of the low doping efficiency of nitrogen acceptors in ZnSe grown by metalorganic chemical vapor deposition. *Applied Physics Letters*, 63:3353, 1993.

[66] J. Wendel, M. Lerch, and W. Laqua. Novel Zirconia-Based Superionic Conductors: The Electrical Conductivity of Y–Zr–O–N Materials. *Journal of Solid State Chemistry*, 142(1):163–167, 1999.

[67] J.S. Lee, M. Lerch, and J. Maier. Nitrogen-doped zirconia: A comparison with cation stabilized zirconia. *Journal of Solid State Chemistry*, 179(1):270–277, 2006.

[68] N. Martin, O. Banakh, A.M.E. Santo, S. Springer, R. Sanjinés, J. Takadoum, and F. Lévy. Correlation between processing and

properties of TiO_xN_y thin films sputter deposited by the reactive gas pulsing technique. *Applied Surface Science*, 185(1-2):123–133, 2001.

[69] A. Magrasó, C. Frontera, D. Marrero-López, and P. Wúñez. Crystal structure determination and characterization of lanthanum tungstate prepared by freeze-drying. 2009. *Submitted*.

[70] M. Kilo, M.A. Taylor, C. Argirusis, G. Borchardt, M. Lerch, O. Kaitasov, and B. Lesage. Nitrogen diffusion in nitrogen-doped yttria stabilised zirconia. *Physical Chemistry Chemical Physics*, 6(13):3645–3649, 2004.

[71] J. Rodriguez-Carvajal. FullProf computer program. *J. Physica B*, 192:55, 1993. Version Feb. 2007.

[72] Pfeiffer Vacuum GmbH. *Mass Spectrometer*, 2002–2004.

[73] T. Norby and P. Kofstad. Electrical Conductivity and Defect Structure of Y_2O_3 as a Function of Water Vapor Pressure. *Journal of the American Ceramic Society*, 67(12):786–792, 1984.

[74] D.C. Harris. *Quantitative chemical analysis*. W.H. Freeman, 6th edition, 2003.

[75] S. Marion, A.I. Becerro, and T. Norby. Ionic and electronic conductivity in $CaTi_{1-x}\ Fe_xO_{3-\delta}$ (x= 0.1–0.3). *Ionics*, 5(5):385–392, 1999.

[76] R.P. Lesunova, E.I. Burmakin, and S.F. Pal'guev. Effect of Calcium Doping on the Electrical Conductivity of Yttrium Nitride. *Inorganic Materials*, 39(5):492–494, 2003.

[77] D. Shibuta, S. Kobayashi, M. Yoshizumi, and H. Arai. Process for preparing a titanium oxide powder, May 26 1987. US Patent 4668501.

[78] M.D. Banus, T.B. Reed, and A.J. Strauss. Electrical and magnetic properties of TiO and VO. *Physical Review B*, 5(8):2775–2784, 1972.

[79] L.E. Toth. Transition Metal Carbides and Nitrides. *Academic Press, NY*, page 90, 1971.

[80] C.L. Perkins, S.H. Lee, X. Li, S.E. Asher, and T.J. Coutts. Identification of nitrogen chemical states in N-doped ZnO via X-ray photoelectron spectroscopy. *Journal of Applied Physics*, 97:034907, 2005.

[81] Z.B. Gu, M.H. Lu, J. Wang, S.T. Zhang, X.K. Meng, Y.Y. Zhu, S.N. Zhu, Y.F. Chen, and X.Q. Pan. Structure, optical, and magnetic properties of sputtered manganese and nitrogen-codoped ZnO films. *Applied Physics Letters*, 88:082111, 2006.

[82] S. Gutzov and M. Lerch. Nitrogen incorporation into pure and doped zirconia. *Ceramics International*, 33(2):147–150, 2007.

[83] Y. Larring and T. Norby. Protons in rare earth oxides. *Solid State Ionics*, 77:147–151, 1995.

[84] M. Mogensen, N.M. Sammes, and G.A. Tompsett. Physical, chemical and electrochemical properties of pure and doped ceria. *Solid State Ionics*, 129(1-4):63–94, 2000.

[85] T. Norby, M. Widerøe, R. Glöckner, and Y. Larring. Hydrogen in oxides. *Dalton Transactions*, 2004(19):3012–3018, 2004.

Appendix A

Flowmeter calibration

The ammonia flowmeter in the gas mixer (section 4.3.2) was calibrated using a *0101-0113 soap film flowmeter* (Hewlett-Packard) and a standard volume of 10 ml. The points in the calibration curve, showed in figure A.1, were taken as a mean of 3–15 measurements depending on the spread of the values. The region between 80–95 mm was not used in flow rate dependencies on conductivity due to the larger deviation in this area.

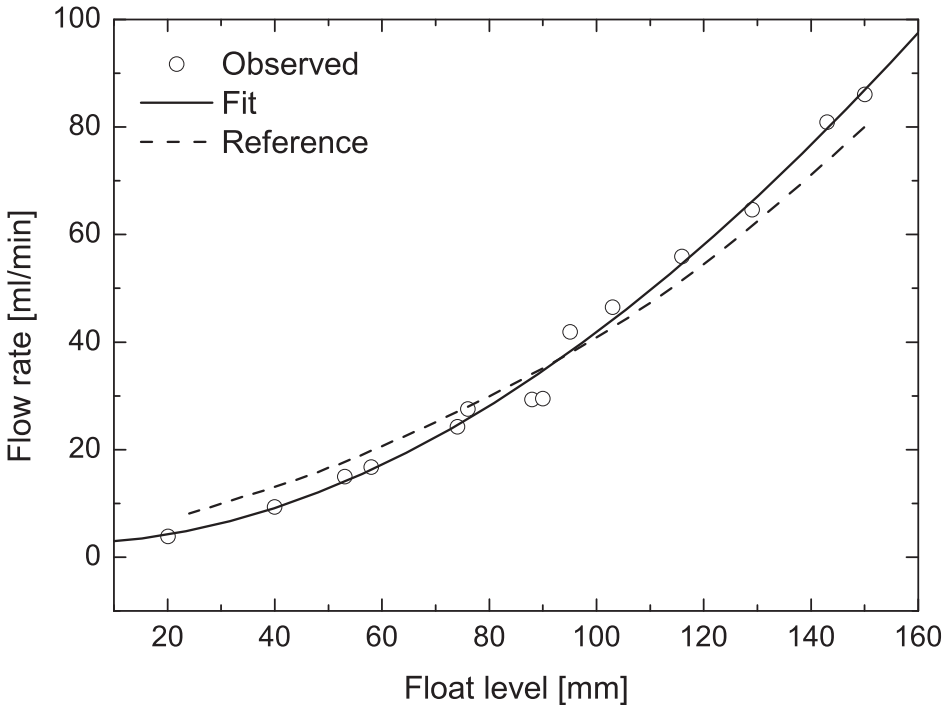

Figure A.1: *Flowmeter calibration curve for ammonia showing the observed values, a 3rd order polynomial fit and the suppliers referance curve. Flow rate is for normal liters (i.e. 1 atm, 25 °C).*

Appendix B

Advanced gas mixer

The gas mixer illustrated in figure B.1 is utilized to establish controlled atmospheres for p_{O_2} and p_{H_2O} dependencies. Oxygen or hydrogen in flowmeter A can be diluted with argon in three stages. The resulting mixture, M3, is humidified or passed directly through to the cell. In the wetting stage, the gas is saturated with water vapor in the first bubbler. Subsequently, the gas is bubbled through a saturated solution of KBr, reducing humidity to 80 % ($p_{H_2O} = 0.025$ atm at 25 °C and 1 atm total pressure). This is done to avoid condensation of water in cooler parts of the apparatus. The ratio between wet and dry gas can be controlled with flowmeters G and H.

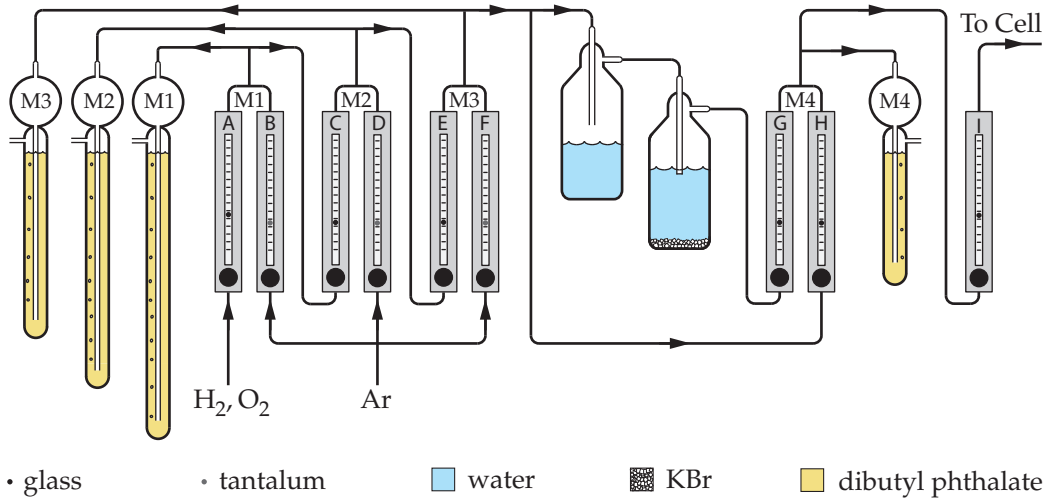

Figure B.1: *Advanced gas mixer unit.*